https://doi.org/10.5194/se-2019-181
Preprint. Discussion started: 2 January 2020

Solid Earth Discussions

Joint inversion of the lithospheric density struture in the North China Craton based on GOCE satellite gravity gradient data and surface gravity data

Yu Tian[1,2,3], Yong Wang[2,3]

[1]Ocean College, Minjiang University, 350108 Fuzhou, China

[2]State Key Laboratory of Geodesy and Earth's Dynamics, Institute of Geodesy and Geophysics, Chinese Academy of Sciences, 430077 Wuhan, China

[3]University of Chinese Academy of Sciences, 100049 Beijing, China

Correspondence to: Yu Tian (tybgys455429145@163.com)

Abstract. The North China Craton (NCC) is one of the oldest cratons in the world. Currently, the destruction mechanism and geodynamics of the NCC still remain controversial. All of the proposed views regarding the issues involve studying the internal density structure of the NCC lithosphere. Gravity field data are one of the most important data in regard to investigating the lithospheric density structure, the gravity gradient data and the gravity data possess their own advantages.

Given the inconsistency of the on orbit GOCE satellite gravity gradient and surface gravity observation plane height, also effects of the initial density model upon of the inversion results, the joint inversion of gravity gradient and gravity are divided into two integrated processes. By using the preconditioned conjugate gradient (PCG) inversion algorithm, the density data are calculated using the preprocessed remaining gravity anomaly data. The newly obtained high resolution density data are then used as the initial density model, which can be served as the constraints for the subsequent gravity gradient inversion. Several essential corrections are performed for the four gravity gradient tensor ($\boldsymbol{T}_{xx}$, $\boldsymbol{T}_{xz}$, $\boldsymbol{T}_{yy}$, $\boldsymbol{T}_{zz}$) of the GOCE satellite, after which the remaining gravity gradient anomaly ($\boldsymbol{T}'_{xx}$, $\boldsymbol{T}'_{xz}$, $\boldsymbol{T}'_{yy}$, $\boldsymbol{T}'_{zz}$) are used as the observation quantity. The result of lithospheric density distribution within the depth range of 0–180km in NCC is obtained .

The inversion results show followings. In the crust, the eastern NCC is affected by the lithosphere thinning with obvious local features. While in the mantle, the presented obvious low density areas are mainly affected by the high heat flux environment. In the eastern NCC, the density anomaly in the Bohai Bay area is mostly attributed to the extension of the Tancheng-Lujiang major fault at the eastern boundary. In the western NCC, the crustal density anomaly distribution of the Qilian block is consistent with the northwest-southeast strike of the surface fault belt, whereas such an anomaly distribution experiences a clockwise rotation nearly to the north-south direction when it enters the mantle.

https://doi.org/10.5194/se-2019-181
Preprint. Discussion started: 2 January 2020

1 Introduction

The North China Craton (Fig.1) is considered to be an outstanding example of cratons that has undergone both reconstruction and destruction. Studies on the NCC have provided us with opportunities to understand its formation and evolution, stabilization and destruction of the ancient continent. Two dominant destruction mechanisms of the NCC have been proposed, namely, delamination (Gao et al., 2009) and thermal erosion (Zhu et al., 2012). However, both of these mechanisms involve internal tectonic deformation and substance distribution of the lithosphere in the NCC, which highlights the utmost importance of obtaining the high resolution density structure of the lithosphere. The most direct and effective approach for investigating the internal density structure is by the gravity field of the Earth. The gravity field data is essential information for studying the laws behind the variations in the gravity field characteristics, which plays an important role in determining and interpreting the Earth's internal structure and state of motion. For studies on the density structure of the NCC, Fang (1996) managed to invert the density distribution of the lithosphere in the North China area, with the constrained least square method using the Bouguer anomaly. Also using the Bouguer gravity anomaly, Wang et al. (2014) obtained the three dimensional density structure of the NCC lithosphere through algebraic reconstruction inversion method, which was constrained by the seismic travel time. Based on the gravity, geoidal surface and topography data, Xu et al. (2016) calculated the crustal density and depth of the interface between the lithosphere and asthenosphere by the rapid integrated inversion method. Using the preprocessed data of the GOCE satellite gravity gradient anomaly, Tian and Wang (2018) constructed a three dimensional density structure within the depth range of 0–120 km of the NCC lithosphere, during which the density variation induced by the temperature differences was incorporated. Previous studies on the NCC only adopted the gravity or gravity gradient measurements, both of which have their own unique advantages as the first order and second order derivatives of the gravity potential, respectively. In the frequency domain, the gravity data can provide mid low frequency information of the deep structure. Therefore, gravity anomalies can be used to reflect the heterogeneity of underground substances of the mid low frequency band. The amplitude of the gravity gradient data declines rapidly with an increasing depth of the field source, which demonstrates that the gravity gradient anomaly is applicable to the corresponding density non-uniformity of the shallow structure, characterized by short wavelengths. By using both the gravity and gravity gradient data as the observation quantities, the low frequency signal information of the gravity anomaly data and the high frequency signal information of the gravity gradient anomaly data can expands the frequency of the gravity field data, which promotes utilization of the available gravity field data. Joint inversion of the gravity and gravity gradient data is able to achieve a mutual supplementation, which is favourable to enhance the reliability of the inversion result and obtain more reasonable analysis of the inversion solutions.

Currently, research based on the joint inversion of the gravity and gravity gradient data is rare. Zhdanov et al. (2004) introduced the concept of the curvature of gravity to carry out an joint inversion of gravity and gravity gradient data, and applied proposed method to the existing models. Wu et al. (2013) realized the inversion combining gravity and gravity

https://doi.org/10.5194/se-2019-181
Preprint. Discussion started: 2 January 2020

gradient by transforming the formulas of the gravity and gravity gradient with the target body treated as a mass point. Given the varied decline rates of the kernel functions of the gravity and gravity gradient data, Capriotti and Li (2014) balanced the two decline rates with the help of the density matrix to conduct an joint inversion of the gravity and gravity gradient data, after which the validity of the proposed method is confirmed using the published SEG model. Qin et al. (2016) developed the integrated focusing inversion algorithm of the gravity and gravity gradient data, and applied this method to the gravity and gravity gradient data of the aerial survey in Vinton salt dome area. Li et al. (2017) inverted the lithospheric three dimensional density structure of the Qinghai-Tibet Plateau and its adjacent area within a depth range of 0–120 km using the gravity gradient data measured by the GOCE L2 together with the vertical gravity calculated via the Earth Gravitational Model (EGM) 2008. In the cases of small research areas, studies involving gravity and gravity gradient joint inversion focused on the applications of the existing models or the aerial gravity and gravity gradient data in local areas at the same height. With respect to previous studies covering a large area, researchers often adopted gravity or gravity gradient data directly computed by the gravity field model. Although the gravity field model is able to rapidly calculate the gravity and gravity gradient data for large research areas all around the world, the resultant data are calculations based on the spherical harmonic coefficient instead of actual measurements. Besides, using the actual observations directly, rather than gravity field models, has the advantages of avoiding the global average effect during gravity field modeling (Pavlis et al., 2012). Thus, compared with the calculated data based on the gravity field model, the high precision gravity and gravity gradient data obtained from actual measurements with high resolution possess same importance (Liu et al., 2003; Li et al., 2011).

So we selected on orbit GOCE satellite gravity gradient data and gravity data of surface survey as the measurements. The GOCE satellite data at the mean orbital height only reflects large structures of the earth. In order to highlight the high frequency information of shallow abnormal bodies and the detailed information of structural features, it is necessary to downward the GOCE satellite data from the mean orbital height to the near surface in NCC area. However, given the feasibility of the downward continuation result of the gravity gradient data from the GOCE satellite, the height of the observation plane after the downward continuation should be located outside the topographic mass unit (Sebera et al., 2014; Li et al., 2017; Tian and Wang, 2018), while the each observation spot for gravity data acquired through the surface survey is always located on the surface of the topographic mass unit. Therefore, a problem of inconsistency in the observation plane height is anticipated between the processed GOCE satellite gravity gradient data and the gravity data obtained by the surface survey. Furthermore, although gravity and gravity gradient data are favoured by higher resolutions and sensitivity to density, the inversion method is characterized by a strong non-uniqueness of solutions. For the purposes of constraining the gravity and gravity gradient inversion, seismic data are often input into the inversion after a transformation based on empirical formulas to suppress the non-uniqueness of solutions. In this regard, the effects of the initial model upon the inversion results should be taken into consideration. For the two aforementioned aspects, the joint inversion of gravity and gravity gradient are divided into two processes. First, the density data converted from the seismic wave velocity are used as the initial density model. The remaining gravity anomaly data of the surface survey in NCC after preprocessing are collected as the

https://doi.org/10.5194/se-2019-181
Preprint. Discussion started: 2 January 2020

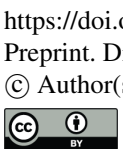

Solid Earth
Discussions
Open Access
EGU

observation quantity, then the density anomaly within a depth range of 0–180 km is calculated using the preconditioned conjugate gradient (PCG) algorithm at the first process. The obtained inversion results are used as the new initial density model, serving as constraints. The four high accuracy (Rummel et al., 2011; Yi et al., 2013) GOCE satellite gravity gradient anomaly tensors (T_{xx} , T_{xz} , T_{yy} , T_{zz}) in NCC are collected as the original observation data for downward continuation, topographic effect correction, underground interface undulation effect correction and long wavelength correction. The preprocessed remaining gravity gradient anomaly data (T'_{xx} , T'_{xz} , T'_{yy} , T'_{zz}) are used as the new observation quantity, the resultant density anomaly distribution within the depth range of 0–180 km in this area are obtained using the same PCG algorithm at the second process. By considering the features of gravity anomaly and gravity gradient anomaly data, we used the remaining gravity data as the initial measurements instead of gravity gradient data, which can be used to determine major and deep structures of the lithosphere by the inversion results firstly. Then the inversion results of remaining gravity gradient data is applied to identify fine structures of the lithosphere. This presented method can be exempt from the limitation imposed by the observation plane height, which is able to sufficiently exploit and utilize the available actual gravity and gravity gradient measurements. The corrected initial model with the effect of the gravity inversion results can provide the more reliable and effective initial density models for the following inversion of the GOCE gravity gradient. Compared with the inversion results based on either the gravity or gravity gradients in the NCC, the integrated inversion results offers both regional details information and density structure model penetrating deeper underground, which is favourable for discussions and analysis of data about the crust and mantle in the same area, consequently, investigating the phenomenon and origin of the destruction mechanism of the NCC.

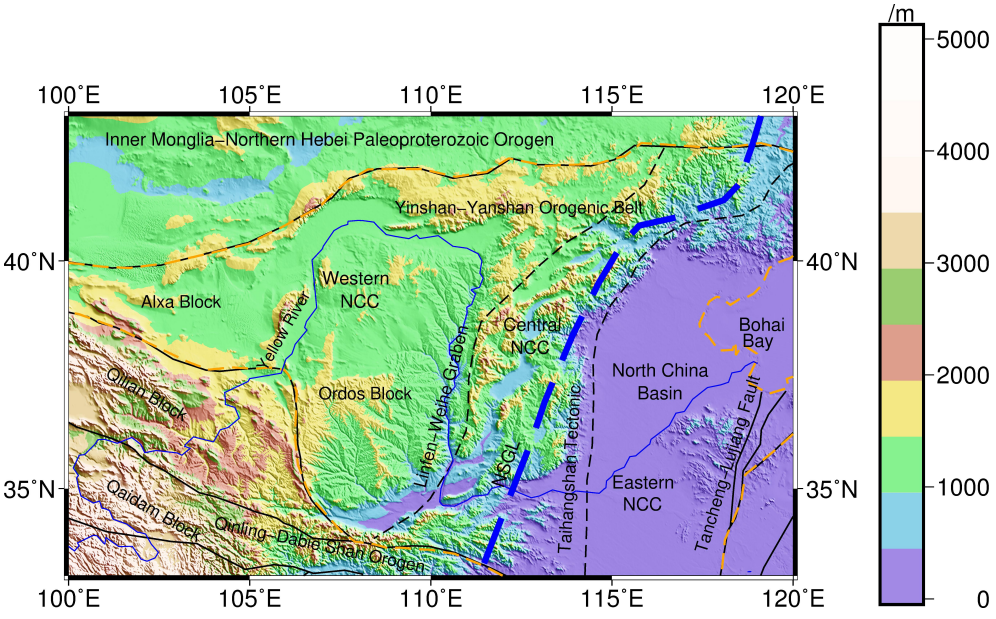

Figure 1 Topography and main tectonics of the study area. NCC - North China Craton.

https://doi.org/10.5194/se-2019-181
Preprint. Discussion started: 2 January 2020

2 Methods

2.1 Inversion method

The inversion of the gravity and gravity gradient tensors is, in essence, a process of solving a system of linear equations. Since the quantity of the unknowns m that need to be calculated, which greatly exceeds the acquired data vector. The inversion is an underdetermined problem, which means the solutions of the equations are non-unique, and appropriate constraints upon the objective function are required to narrow the range of solutions. Therefore, in the linear inversion theory, the objective function mostly consists of the data fitting function and the model objective function (Constable et al., 1987). Under such circumstances, solving the inversion problem is equivalent to finding a model vector $\boldsymbol{m}$ that is able to minimize the objective function while satisfying the data fitting function condition.

The objective function can be expressed as:

$$\text{minimize } :\phi = \phi_d + \mu\phi_m , \tag{1}$$

where μ represents the regularization parameter, which stands for the weight factor that balances the data fitting function ϕ_d and the model objective function ϕ_m.

The data fitting function is defined as below:

$$\phi_d = \sum_{i=1}^{N}\left(\frac{\Delta \boldsymbol{d}_i - \boldsymbol{G}_i\Delta \boldsymbol{m}}{\sigma_i}\right)^2 = \left\|\boldsymbol{W}_d(\Delta \boldsymbol{d} - \boldsymbol{G}\Delta \boldsymbol{m})\right\|^2 , \tag{2}$$

$$\boldsymbol{W}_d = diag\left\{1/\sigma_1 , 1/\sigma_2 , ..., 1/\sigma_N\right\}, \tag{3}$$

where $\Delta \boldsymbol{m}=\boldsymbol{m}-\boldsymbol{m}_0$ is the correction between the model parameter vector $\boldsymbol{m}$ and the initial model $\boldsymbol{m}_0$; $\boldsymbol{G}$ is the kernel function, namely, the linear projection operator from the model element to the observation(for gravity data, $\boldsymbol{G}$ is the corresponding kernel function in the gravity inversion, while for gravity gradient components, it is the corresponding kernel function used in the gravity gradient inversion); $\Delta \boldsymbol{d}$ is the correction of the corresponding measurement; and $\boldsymbol{W}_d$ is a diagonal matrix, with σ_i representing the standard deviation of the *i*-th data. The objective function of the model is constructed according to the minimization model function, which is expressed as minimize: $\left\|\Delta \boldsymbol{m}\right\|^2 = \int \Delta \boldsymbol{m}^2 \mathrm{d}v$.

The Lagrangian multiplier is used as the regularization parameter in the PCG inversion algorithm. In the process of solving a large scale matrix, calculation of the Lagrangian multiplier is comprehensive, therefore, an empirical value is often adopted as the relative optimal value for the regularization parameter. Since the regularization parameter serves to balance the data fitting function and the model fitting function, an excessively large value will result in substantial differences between the

https://doi.org/10.5194/se-2019-181
Preprint. Discussion started: 2 January 2020

model response and the measurement value, while an overwhelmingly small value leads to a discrepancy between the model and the reality and, consequently, unreliable inversion results. Given these problems, the value corresponding to the inflection point of the L curve is assigned to the regularization parameter. The L curve is a criterion that is based on a comparison between the actual data fitting function and the model objective function, which is applicable to solving problems with large scales. The effectiveness of this method has been validated in previous studies (Tian et al., 2018; 2019). The curvature of the L curve can be expressed as (Hansen, 1992):

$$k = \frac{\hat{\rho}'\hat{\eta}'' - \hat{\rho}''\hat{\eta}'}{\left[(\hat{\rho}')^2 + (\hat{\eta}')^2\right]^{3/2}}, \tag{4}$$

where $\hat{\rho} = \log(\phi_d)$, $\hat{\eta} = \log(\phi_m)$; and the superscripts ' and " represent the first-order and second-order derivatives of the function, respectively. Accordingly, during the inversion process, the algorithm seeks the maximum curvature of the L curve based on the function constructed by actual data.

To constrain the spatial structure of the model and achieve a continuous variation of the inversion image along the three axis directions, a roughness matrix is introduced into the model objective function (Constable et al., 1987), with reference to the minimization model function. The three dimensional model vector $\boldsymbol{R}$ is the quadratic sum of the first-order partial difference of the model vector $\boldsymbol{m}$ along the x, y and z directions.

$$\boldsymbol{R} = \left\|\partial_x \Delta\boldsymbol{m}\right\|^2 + \left\|\partial_y \Delta\boldsymbol{m}\right\|^2 + \left\|\partial_z \Delta\boldsymbol{m}\right\|^2 = \int\left(\frac{\partial\Delta\boldsymbol{m}}{\partial x}\right)^2 dv + \int\left(\frac{\partial\Delta\boldsymbol{m}}{\partial y}\right)^2 dv + \int\left(\frac{\partial\Delta\boldsymbol{m}}{\partial z}\right)^2 dv, \tag{5}$$

by meshing the model and replacing the partial differential form with the finite difference form, the above equation is converted into the matrix :

$$\boldsymbol{R} = \Delta\boldsymbol{m}(\boldsymbol{R}_x^{\mathrm{T}}\boldsymbol{R}_x + \boldsymbol{R}_y^{\mathrm{T}}\boldsymbol{R}_y + \boldsymbol{R}_z^{\mathrm{T}}\boldsymbol{R}_z)\Delta\boldsymbol{m}, \tag{6}$$

where $\boldsymbol{R}_x$、$\boldsymbol{R}_y$ and $\boldsymbol{R}_z$ are the roughness matrices of the model along the x, y and z directions, respectively.

Because the gravity data and gravity gradient data has no fixed depth resolution, the kernel function declines rapidly with an increasing depth, and the inversion results are limited near the surface, which results in difficulties in capturing the true position of the anomaly. By introducing the depth weighting function into the model objective function, the kernel function is optimized to reflect the true weighted value of the anomaly element at each depth. The depth weighting function designed by Li and Oldenburg (1996) especially for the inversion of gravity data and gravity gradient data is adopted:

$$\boldsymbol{W}(z) = \frac{1}{(Z + Z_0)^{\beta/2}}, \tag{7}$$

where Z is the burial depth of the centre of the grid cell; Z_0 and β are constants. For gravity data, these values are used to counteract the decline in the kernel function $\boldsymbol{G}$, with β often set to 2 and the function written as $(Z+Z_0)^{-1}$, while for gravity

https://doi.org/10.5194/se-2019-181
Preprint. Discussion started: 2 January 2020

Solid Earth Discussions

gradient data, these values are used to compensate the decline in the kernel function $\boldsymbol{G}$, with β often set to 3 and the function written as $(Z+Z_0)^{-3/2}$.

In accordance with the minimization model function, the model objective function can be constructed as shown below, in reference to the roughness matrix and depth weighting function:

$$\phi_m(\boldsymbol{m}) = \alpha_s \int_V (\partial \boldsymbol{W}(z)\Delta\boldsymbol{m})^2 dv + \alpha_x \int_V \left(\frac{\partial \boldsymbol{W}(z)\Delta\boldsymbol{m}}{\partial x}\right)^2 dv + \alpha_y \int_V \left(\frac{\partial \boldsymbol{W}(z)\Delta\boldsymbol{m}}{\partial y}\right)^2 dv + \alpha_z \int_V \left(\frac{\partial \boldsymbol{W}(z)\Delta\boldsymbol{m}}{\partial z}\right)^2 dv, \quad (8)$$

the model objective function can be converted into the matrix form by replacing the differential form with the finite difference method:

$$\phi_m(\boldsymbol{m}) = \Delta\boldsymbol{m}^{\mathrm{T}}(\boldsymbol{W}_S^{\mathrm{T}}\boldsymbol{W}_S + \boldsymbol{W}_x^{\mathrm{T}}\boldsymbol{W}_x + \boldsymbol{W}_y^{\mathrm{T}}\boldsymbol{W}_y + \boldsymbol{W}_z^{\mathrm{T}}\boldsymbol{W}_z)\Delta\boldsymbol{m} = \Delta\boldsymbol{m}^{\mathrm{T}}\boldsymbol{W}_i^{\mathrm{T}}\boldsymbol{W}_i\Delta\boldsymbol{m}, \quad (9)$$

$$\boldsymbol{W}_i = \alpha_i \boldsymbol{R}_i \boldsymbol{D}, \quad i = s, x, y, z, \quad (10)$$

where α_i is the weight coefficient for each term in the objective function; $\boldsymbol{R}_i$ is the difference operator for each component; and $\boldsymbol{D}$ is the discretized depth weighting function matrix. Substituting the model objective function into the objective function yields:

$$\phi = (\Delta\boldsymbol{d} - \boldsymbol{G}\Delta\boldsymbol{m})^{\mathrm{T}}(\Delta\boldsymbol{d} - \boldsymbol{G}\Delta\boldsymbol{m}) + \mu\,\Delta\boldsymbol{m}^{\mathrm{T}}\boldsymbol{W}_i^{\mathrm{T}}\boldsymbol{W}_i\Delta\boldsymbol{m}, \quad (11)$$

Eq. (11) can be re-arranged into the form of matrix:

$$\begin{bmatrix} \boldsymbol{G} \\ \sqrt{\mathrm{k}}\boldsymbol{W}_{\mathrm{i}} \end{bmatrix} \Delta\boldsymbol{m} = \begin{bmatrix} \Delta\boldsymbol{d} \\ 0 \end{bmatrix}, \quad (12)$$

by replacing the condition matrix of the objective function with $\boldsymbol{A} = \begin{bmatrix} \boldsymbol{G} \\ \sqrt{k}\boldsymbol{W}_{\mathrm{i}} \end{bmatrix}$ and defining $\boldsymbol{b} = \begin{bmatrix} \Delta\boldsymbol{d} \\ 0 \end{bmatrix}$, Eq. (12) can be simplified as:

$$\boldsymbol{A}\Delta\boldsymbol{m} = \boldsymbol{b}, \quad (13)$$

for the gravity data, we take the $\boldsymbol{T}_{\mathrm{z}}$ as the observation, $\boldsymbol{A} = \begin{bmatrix} \boldsymbol{G}_z \\ \sqrt{\mu}\boldsymbol{W}_{\mathrm{i}} \end{bmatrix}$ and $\boldsymbol{b} = \begin{bmatrix} \boldsymbol{T}_{\mathrm{z}} \\ 0 \end{bmatrix}$, for the gravity gradient data, we selected four processed components $\boldsymbol{T}_{xx}$、$\boldsymbol{T}_{xz}$、$\boldsymbol{T}_{yy}$ and $\boldsymbol{T}'_{zz}$ as the observation, which implies the Jacobian

https://doi.org/10.5194/se-2019-181
Preprint. Discussion started: 2 January 2020

matrix $\boldsymbol{A}=\begin{bmatrix} \boldsymbol{G}_{xx} \\ \boldsymbol{G}_{xz} \\ \boldsymbol{G}_{yy} \\ \boldsymbol{G}_{zz} \\ \sqrt{\mu}\boldsymbol{W}_i \end{bmatrix}$ and $\boldsymbol{b}=\begin{bmatrix} \boldsymbol{T}'_{xx} \\ \boldsymbol{T}'_{xz} \\ \boldsymbol{T}'_{yy} \\ \boldsymbol{T}'_{zz} \\ 0 \end{bmatrix}$. Additionally, $\boldsymbol{A}^{\mathrm{T}}\boldsymbol{A}=(\boldsymbol{G}^{\mathrm{T}}\boldsymbol{G}+k^{-1}\boldsymbol{W}_i^{\mathrm{T}}\boldsymbol{W}_i)$. Because the condition number of the Jacobian matrix is normally very large, to increase the convergence speed and the solution stability, Eq. (13) is re-written as:

$$\boldsymbol{S}\boldsymbol{A}^{\mathrm{T}}\boldsymbol{A}\Delta\boldsymbol{m}=\boldsymbol{S}\boldsymbol{A}^{\mathrm{T}}\boldsymbol{b}, \tag{14}$$

where $\boldsymbol{S}$ is the preconditioned factor and is usually approximated as $(\boldsymbol{A}^{\mathrm{T}}\boldsymbol{A})^{-1}$. By doing this, the eigenvalues of Eq. (14) will be concentrated along the diagonal and the condition number will be improved so that the iteration efficiency is improved (Pilkington, 2009).

The PCG method is an algorithm for solving linear or nonlinear equations through an iterative calculation process and is mainly used to solve a quadratic equation $\phi=\frac{1}{2}\boldsymbol{m}^{\mathrm{T}}\boldsymbol{A}\boldsymbol{m}-\boldsymbol{m}^{\mathrm{T}}\boldsymbol{b}$, with the solution $\boldsymbol{m}=\boldsymbol{A}^{-1}\boldsymbol{b}$, which obviously is equivalent to Eq. (13). This algorithm adopts the gradient of the initial point as the starting conjugate direction. It is along this direction, instead of the non-negative gradient direction, that the algorithm searches for minimal points of the objective function to improve the stability of the solution (Pilkington, 1997; 2009). The $\boldsymbol{m}$ of the model is calculated in accordance with the PCG inversion algorithm, and whether or not the inversion proceeds is determined according to the value of residual mean square at every iteration step. When the resultant $\boldsymbol{m}$ of the model satisfies the prescribed relative fitting difference, RMS, the iterative calculation of the inversion is considered to be complete.

The relative fitting difference in the inversion algorithm is defined as:

$$\mathrm{RMS}=\sqrt{\frac{\sum_{i=1}^{\mathrm{N}}\left[\left(\boldsymbol{d}_{\mathrm{i}}^{\mathrm{obs}}-\boldsymbol{d}_{\mathrm{i}}^{\mathrm{fwd}}\right)/\boldsymbol{d}_{\mathrm{i}}^{\mathrm{obs}}\right]^2}{\mathrm{N}}}, \tag{15}$$

where N is the quantity of the measurement; $\boldsymbol{d}_{\mathrm{i}}^{\mathrm{obs}}$ is the measured value; and $\boldsymbol{d}_{\mathrm{i}}^{\mathrm{fwd}}$ is the theoretical value corresponds to inversion model.

The detailed calculation process of the PCG algorithm is stated as follows:

(1) The measurement $\boldsymbol{d}^{\mathrm{obs}}$ and the initial model $\boldsymbol{m}_0^{\mathrm{k}}$ are known, where k = 1, 2, $\cdots N_{\max}$ and $N_{\max}$ represents the maximum iteration quantity of the external circulation.

https://doi.org/10.5194/se-2019-181
Preprint. Discussion started: 2 January 2020

(2) Calculate the difference between the measurement data and the theoretical data computed from the initial model $\Delta \boldsymbol{d}^{k} = \boldsymbol{d}^{obs} - \boldsymbol{G}\boldsymbol{m}_0^{k}$, and $\boldsymbol{r}_0 = \boldsymbol{A}^{T}(\boldsymbol{b} - \boldsymbol{A}\Delta\boldsymbol{m}_0^{k})$.

(3) The initial variables are defined as: $\boldsymbol{A} = [\boldsymbol{G}\ \sqrt{k^{-1}}\boldsymbol{W}_i\ ]^{T}$, $\boldsymbol{b}^{k} = [\Delta\boldsymbol{d}^{k}\ \ 0\ ]$, $\Delta\boldsymbol{m}_0^{k} = 0$, $\boldsymbol{z}_0 = \boldsymbol{S}\boldsymbol{r}_0$ and $\boldsymbol{p}_0 = \boldsymbol{z}_0$.

(4) Set i = 1, 2, $\cdots N_{CG\max}$, where $N_{CG\max}$ is the maximum iteration quantity of the internal loop, and carry out computation of the PCG algorithm, where $\boldsymbol{q}_i = \boldsymbol{A}\boldsymbol{p}_i$, $\boldsymbol{\alpha}_i = (\boldsymbol{r}_{i-1}^{T}\boldsymbol{z}_{i-1})/\boldsymbol{q}_i^{T}\boldsymbol{q}_i$, $\Delta\boldsymbol{m}_i^{k} = \Delta\boldsymbol{m}_{i-1}^{k} + \boldsymbol{\alpha}_i\boldsymbol{p}_i$, $\boldsymbol{r}_i = \boldsymbol{r}_{i-1} - \boldsymbol{\alpha}_i\boldsymbol{A}^{T}\boldsymbol{q}_i$, and $\boldsymbol{z}_i = \boldsymbol{S}\boldsymbol{r}_i$. $\boldsymbol{S}$ represents the preconditioned matrix, $\boldsymbol{z}_i$ is the improved search direction; $\boldsymbol{\beta}_i = (\boldsymbol{r}_i^{T}\boldsymbol{z}_i)/\boldsymbol{r}_{i-1}^{T}\boldsymbol{z}_{i-1}$; and $\boldsymbol{p}_i = \boldsymbol{z}_{i-1} + \boldsymbol{\beta}_i\boldsymbol{p}_{i-1}$.

(5) Upon calculating the internal loop of the PCG inversion, set $\boldsymbol{m}_1^{k} = \boldsymbol{m}_0^{k} + \Delta\boldsymbol{m}^{k}$.

(6) Set $\boldsymbol{m}_0^{k} = \boldsymbol{m}_1^{k}$, re-construct the initial model and return to Step (2). Continue the iteration until the convergence condition is met.

2.2 Effects of the initial density model

Two models(Fig.2 and Fig.3) are designed in order to further test the effects of the initial model upon the inversion results. The model one(Fig. 2) consists of two independent cubes, which is relatively simple. The density value of the anomalies is different at each layer, which is primarily used to identify the effect of the initial model upon the density value of the anomaly. The model two(Fig. 3), composed of an upright cuboid and a trapezoid structure of multiple anomalies, which is mainly used to illustrate the effects of the initial model upon the shape and magnitude of the inversion results. Since this study aims to capture the effects of the initial density model upon the final inversion results, carrying out the integrated inversion for the four components ($\boldsymbol{T}_{xx}$, $\boldsymbol{T}_{xz}$, $\boldsymbol{T}_{yy}$, $\boldsymbol{T}_{zz}$) is required.

As is shown in Fig. 2 and Fig. 3, the inversion has been carried out for the identical density anomaly bodies (Fig. 2a and Fig. 3a), during which the gravity gradient measurement, kernel function and algorithm parameters are all the same, except that the varied values are assigned to the initial model. In Model 1, the anomalies are set to 0 g/cm^3 (Fig. 2b); 0.4 g/cm^3 (Fig. 2c); 0.1 g/cm^3 (the 1st layer), 0.2 g/cm^3 (the 2nd and 3rd layers) and 0.3 g/cm^3 (the 4th layer) in Fig. 2d; 0.2 g/cm^3 (the 1st layer), 0.4 g/cm^3 (the 2nd and 3rd layers) and 0.6 g/cm^3 (the 4th layer) in Fig. 2e. Then, in Model 2, the initial densities are set as 0 g/cm^3 (Fig. 3b), 0.2 g/cm^3 (Fig. 3c), 0.5 g/cm^3 (Fig. 3d) and -0.2 g/cm^3 (Fig. 3e).

In terms of the inversion of Model 1, the iterations are 10, 7, 6 and 3, and the inversion results are illustrated in Fig. 2b-e. The detailed results of every inversion test are summarized in Table 1.

https://doi.org/10.5194/se-2019-181
Preprint. Discussion started: 2 January 2020

Solid Earth Discussions

Table 1 Conditions and results for initial density model one.

	Initial density (g/cm^3) (1^{st} to 4^{th} layer)	Iterations (k)	Maximum density at each layer (g/cm^3) (1^{st} to 4^{th} layer)	Minimum density at each layer (g/cm^3) (1^{st} to 4^{th} layer)	Average density at each layer(g/cm^3) (1^{st} to 4^{th} layer)
Test 1	(0, 0, 0, 0)	10	(0.34, 0.42, 0.53, 0.55)	(0.23, 0.27, 0.34, 0.29)	(0.31, 0.34, 0.41, 0.35)
Test 2	(0.4, 0.4, 0.4, 0.4)	7	(0.51, 0.55, 0.66, 0.58)	(0.42, 0.43, 0.51, 0.48)	(0.47, 0.50, 0.58, 0.55)
Test 3	(0.1, 0.2, 0.2, 0.3)	6	(0.36, 0.64, 0.67, 0.64)	(0.32, 0.46, 0.33, 0.55)	(0.34, 0.55, 0.59, 0.58)
Test 4	(0.2, 0.4, 0.4, 0.7)	3	(0.38, 0.72, 0.76, 0.95)	(0.33, 0.52, 0.57, 0.83)	(0.35, 0.59, 0.65, 0.91)

Fig. 2b–e indicate that as the initial model becomes more precise, the inversion results become more reliable, with the values of the anomalies become more similar to the true model. With no defined initial model (Fig. 2b), it is difficult to capture the layered structure of the anomaly and the resultant average density is only 0.38 g/cm^3, which is far different from the true model, although in this case, the inversion results manage to capture the position of the anomaly, its depth distribution, and its shape as two upright cuboids. The whole inversion process is relatively time consuming and finally reaches the convergence criterion after 10 iterations. We also compare the cases based on Model 1 with one another. Compared with Fig. 2d, although Fig. 2c presents smaller differences of the density anomaly values from those of the true model, the layered structure of the anomaly is difficult to capture from Fig. 2c. In Fig.2d, it is feasible to conclude that certain differences exist between the density anomaly distributions of the 1^{st} and 2^{nd} layers, which is more similar to the true model. This finding suggests that the inversion results are related not only to the density value of the initial model but also to the distribution structure of the initial density. Therefore, a more precise initial model with a layered density value distribution is in favour of generating more reliable inversion results. It should be noted that the optimal inversion results are attributed to the case of Fig. 2e, which produce an inverted anomaly body shape that is almost identical to the true model. Apparently, the density distribution of the anomaly body is laminated into 3 layers, with the 1^{st} layer having a density anomaly of 0.3–0.4 g/cm^3; the 2^{nd} and 3^{rd} layers generally having density anomalies of 0.6–0.7 g/cm^3; and the 4^{th} layer having a density anomaly of 0.8–1.0 g/cm^3.

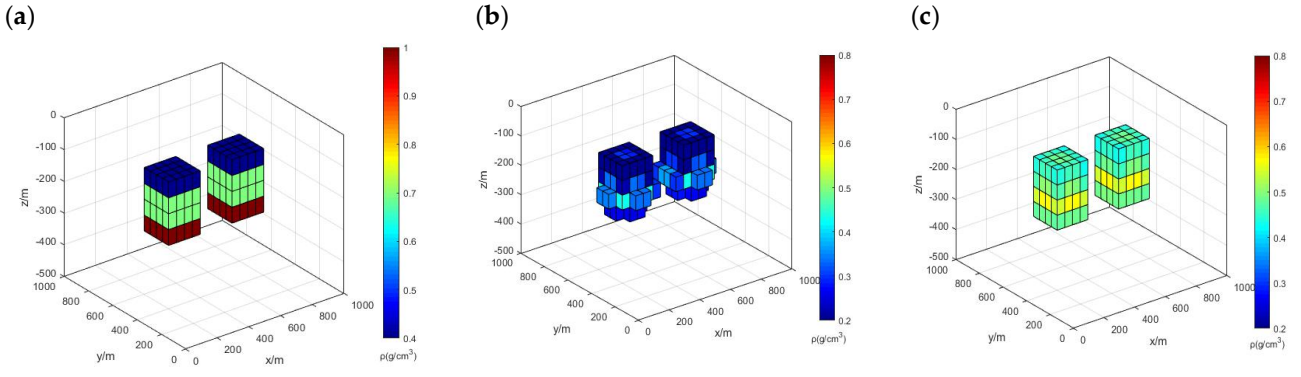

https://doi.org/10.5194/se-2019-181
Preprint. Discussion started: 2 January 2020

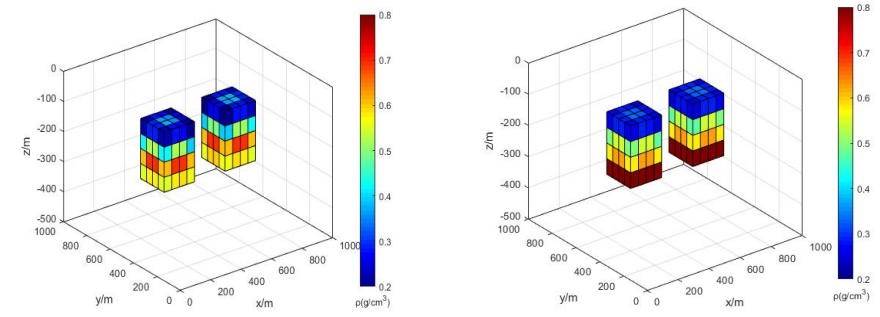

Figure 2 Initial density model experiments one. (**a**)Real model. (**b**)Inversion result (Test 1) without initial density value. (**c**)Inversion result (Test 2) with 0.4 g/cm^3 initial density value at all layers for anomalies. (**d**)Inversion result (Test 3) with 0.1 g/cm^3 , 0.2 g/cm^3, 0.3 g/cm^3 initial density value at 1st, 2nd or 3rd, 4th layer for anomalies. (**e**)Inversion result (Test 4) with 0.2 g/cm^3 , 0.4 g/cm^3, 0.6 g/cm^3 initial density value at 1st, 2nd or 3rd, 4th layer for anomalies.

For Model 2, the inversion for each case is calculated after 8, 7, 5 and 13 iterations. The inversion results are illustrated in Fig. 3b–e, and the details of the results of each case are concluded in Table 2. Fig. 3b–d demonstrate that it would be easier to determine the shape and dimensions of the density anomaly body from the inversion results with the help of a more precise initial model. In the inversion results of Fig. 3b, it is feasible to directly capture the right upright cuboid of the density anomaly, and for the left complicated density anomaly body, the interpretation based on the inversion results is limited to this anomaly body having an irregular shape and its size growing with an increasing depth. In Fig. 3c, the left anomaly body reveals a stair-like shape, yet it is surrounded by multiple small anomaly bodies, and the density values of the right upright cuboid are closer to the true model. Next, the optimal inversion results are found in Fig. 3d, with the anomaly body shapes that are completely consistent with those of the true model, and it is easy to discriminate the shape of the anomaly body. Meanwhile, it should also be noted that the density anomaly value of the right upright cuboid is higher than that of the left stair-like body. Finally, the inversion results of Fig. 3e show difficulties in determining the shape and size of both of the anomaly bodies. In addition, according to the inversion results summary (Table 2), the average density anomaly in this case is only 0.3276 g/cm^3, which is very different from the true model.

Table 2 Conditions and results for initial density model two.

	Initial density (g/cm^3)	Iterations (k)	Maximum density (g/cm^3)	Minimum density (g/cm^3)	Average density (g/cm^3)
Test 5	0	8	0.6887	0.1328	0.4225
Test 6	0.2	7	0.7121	0.1856	0.4886
Test 7	0.5	5	0.7556	0.4762	0.6256
Test 8	-0.2	13	0.6399	0.0399	0.3276

https://doi.org/10.5194/se-2019-181
Preprint. Discussion started: 2 January 2020

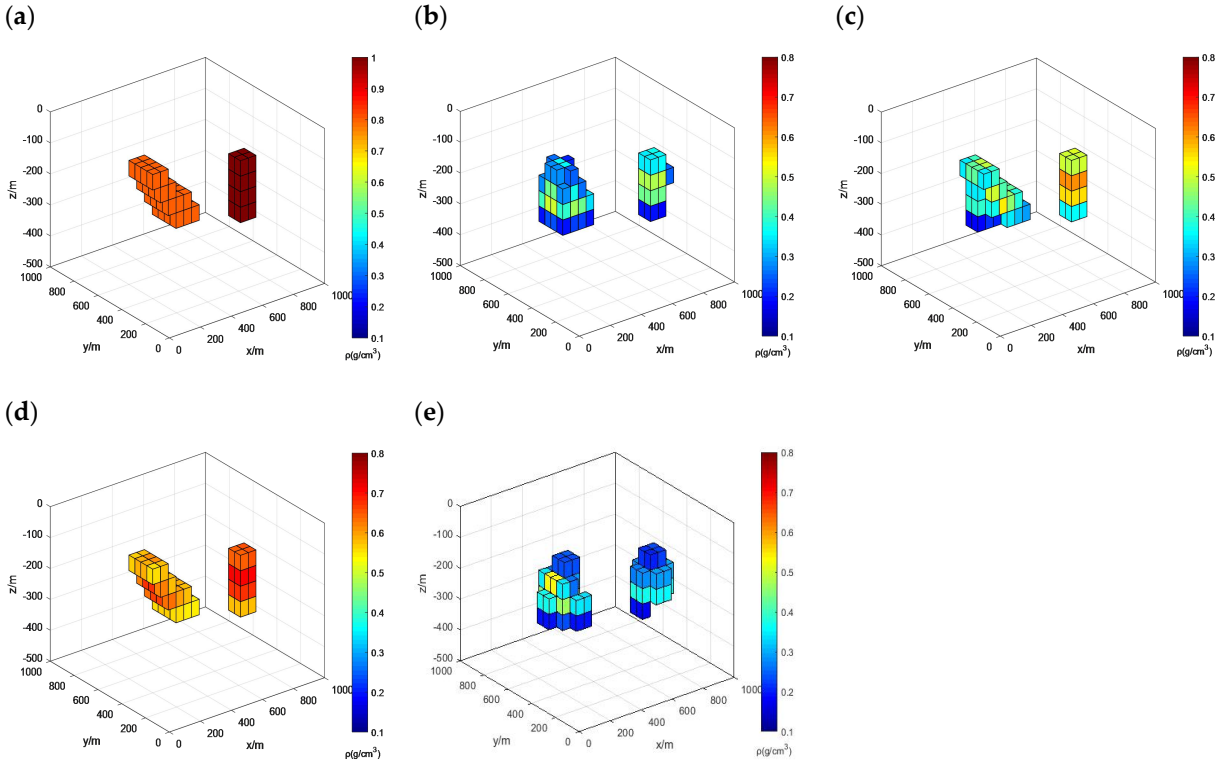

Figure 3 Initial density model experiments two. (**a**)Real model. (**b**)Inversion result (Test 5) without initial density value. (**c**)Inversion result (Test 6) with 0.2 g/cm^3 initial density value for anomalies. (**d**)Inversion result (Test 7) with 0.5 g/cm^3 initial density value for anomalies. (**e**)Inversion result (Test 8) with -0.2 g/cm^3 initial density value for anomalies.

The model tests show that the inversion results are not only related to the observation, but also affected by the physical and geometric parameters of the initial density model. Therefore, the density values for the initial model, as well as the general area where the density anomaly body is located, should be set more accurate for the initial density model. When we obtain more accurate initial density models, combined with the advantages of the high resolution gravity gradient data, it will be more conducive to discussions of the anomaly bodies distribution in the local area.

2.3 The process of the joint inversion

The joint inversion is decomposed into two integrated processes, namely, the gravity inversion and the gravity gradient inversion. The detailed work-flow of the whole inversion process is illustrated in Fig. 4. Given the constraint imposed on the inversion results by the initial density model, the results of the gravity inversion with high precision are used as the new initial density model for the subsequent steps, by which the ultimate inversion results are, to some extent, constrained during the gravity gradient inversion calculation. Specifically, the density data converted from the seismic wave velocity are first

https://doi.org/10.5194/se-2019-181
Preprint. Discussion started: 2 January 2020

used as the initial density model, and the preprocessed remaining gravity anomaly data are collected to serve as the observation quantity. Then, the kernel function corresponding to the gravity data is calculated, and the density anomaly data within the depth range of 0–180 km in the study area are calculated through the PCG algorithm. Then, the obtained gravity inversion results are used as the new initial density model and the gravity gradient components of this area measured by the GOCE satellite are processed, after which the remaining gravity gradient anomaly components are used as the new observation. The kernel functions corresponding to each gravity gradient component are calculated, and then the ultimate density anomaly distribution within a depth range of 0–180 km in the study area is obtained through the same PCG algorithm.

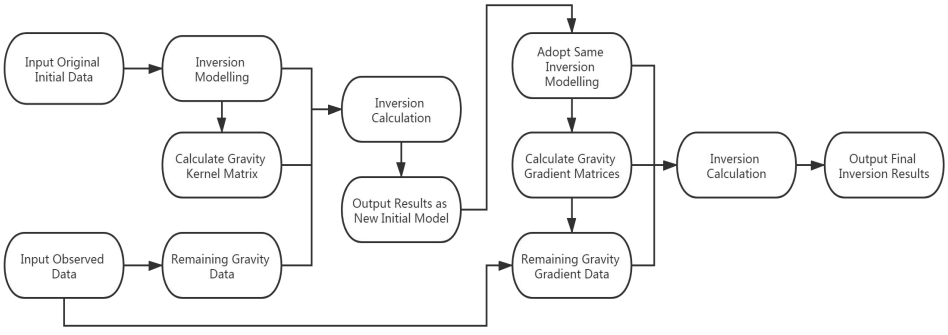

Figure 4 The flowchart of the whole procedure of the PCG inversion algorithm.

3 Data processing

3.1 Inversion based on the remaining gravity anomaly data

The remaining gravity anomaly data(Wang et al., 2012) of the study area after the topographic correction, Bouguer correction, interface undulation correction and long wavelength correction have been directly collected. The spatial resolution of the remaining gravity anomalies data is 5 arc-min. The gravity anomalies induced by the density heterogeneity of the lithosphere are used as the observation for inversion. The remaining gravity anomaly (Fig. 5a) after multiple corrections are shown in Fig. 5a. The figure shows that the gravity anomaly of the eastern NCC is seen with alternating distributions of positive and negative anomalies on an overall basis, with no prominent local features. Nevertheless, obvious differences in the gravity anomaly distributions are found between the two sides of the Tancheng-Lujiang fault belt. In the east of the Tancheng-Lujiang fault belt, the gravity anomaly is dominantly positive, while on the western side, it is primarily negative. In the central NCC, most regions along the Taihang Orogenic belt and the Yinshan-Yanshan Orogenic belt are found with negative gravity anomalies. For the western NCC, the whole Ordos block presents a prominent positive gravity anomaly distribution.

https://doi.org/10.5194/se-2019-181
Preprint. Discussion started: 2 January 2020

Solid Earth
Discussions
Open Access
EGU

Although the gravity data are favoured by their higher resolutions, the gravity inversion suffers from a strong non-uniqueness of solutions. It is effective to introduce seismic data into the gravity inversion to constrain the gravity inversion process the non-uniqueness of solution. Based on the resolution of 0.5°×0.5° P-wave velocity structure obtained by seismic tomography (Tian et al., 2009), we constructs a three dimensional initial density model for the NCC lithosphere, using the empirical velocity to density conversion formula of the North China area (Eq. 16). The constructed models is divided into eight layers along the depth direction, with base depths of 10 km, 25 km, 42 km, 60 km, 80 km, 100 km, 140 km and 180 km. Along the horizontal direction, the model is meshed into grids of 0.25° × 0.25° . As shown in Fig. 5b, after 17 outer iterations, the curve of defined RMS misfit tends to be horizontal, the variation is slight, and the calculated RMS misfit of 8.2×10^{-3} was obtained, at which point the inverse iterative calculation was complete.

(a) **(b)**

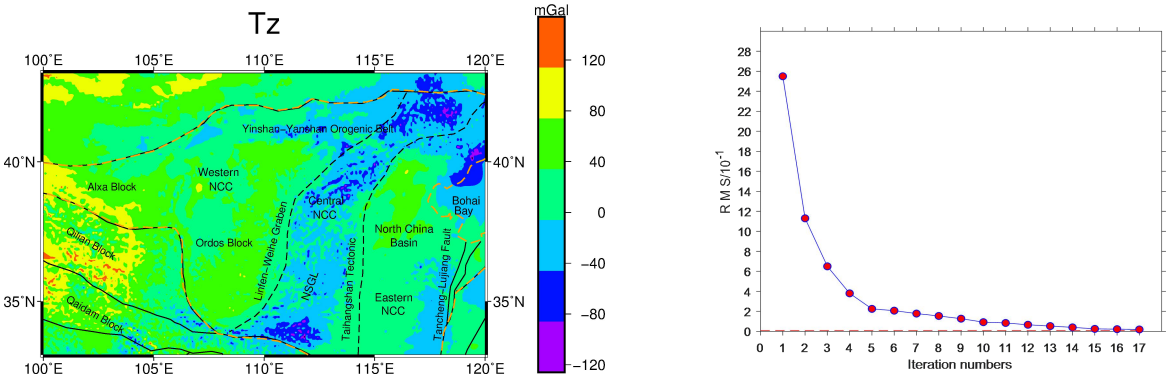

Figure 5 (**a**)Remaining gravity anomalies after several corrections. (**b**)With the iterative calculation, residual mean square between the forward calculated theoretical gravity and the gravity measurements versus iteration number in the PCG inversion algorithm, the red line represents the rms value of 0.01.

The three-dimensional density anomaly distribution of the lithosphere within 0–180 km, which is meshed into 0.25° × 0.25° cells (Fig. 6), has been inverted from the remaining gravity anomaly. The results are then used as the new initial model for the gravity gradient inversion. In Sect. 5, the results of the initial and final inversion results (Fig.6 and Fig.15) are further analysed and discussed.

https://doi.org/10.5194/se-2019-181
Preprint. Discussion started: 2 January 2020

Solid Earth
Discussions
Open Access
EGU

(a)

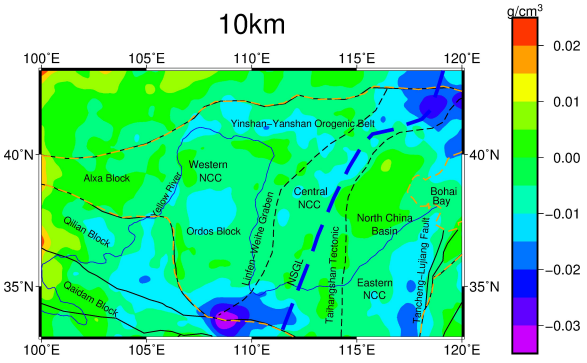

(b)

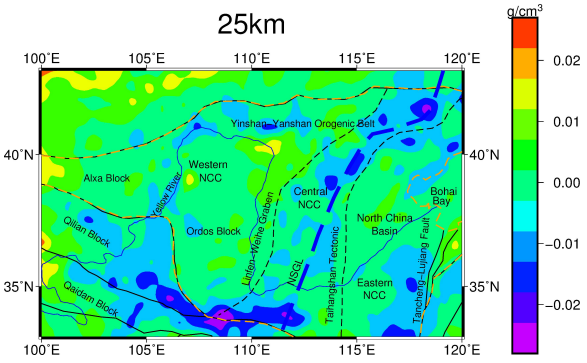

(c)

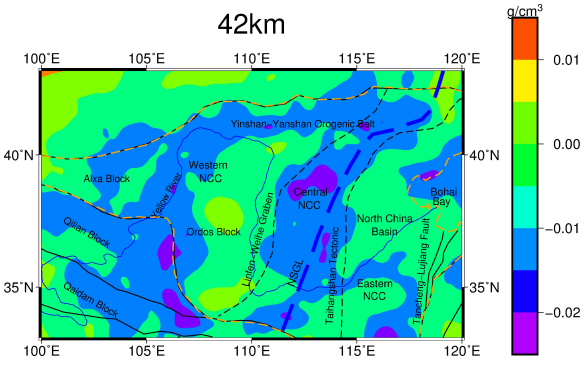

(d)

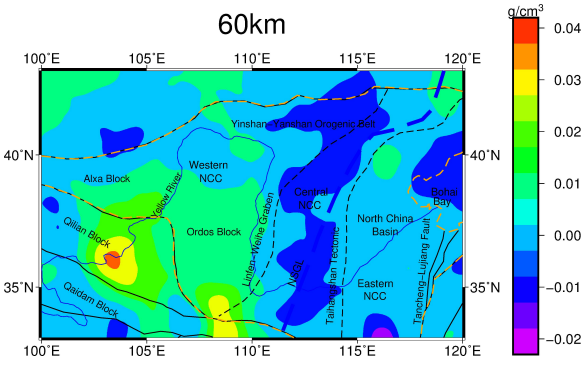

(e)

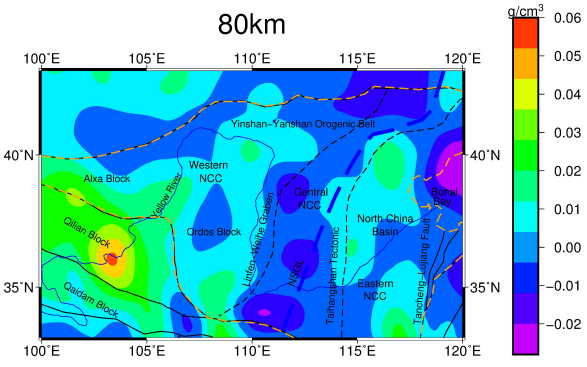

(f)

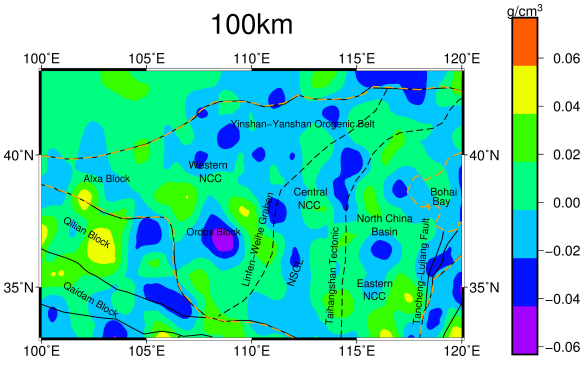

https://doi.org/10.5194/se-2019-181
Preprint. Discussion started: 2 January 2020

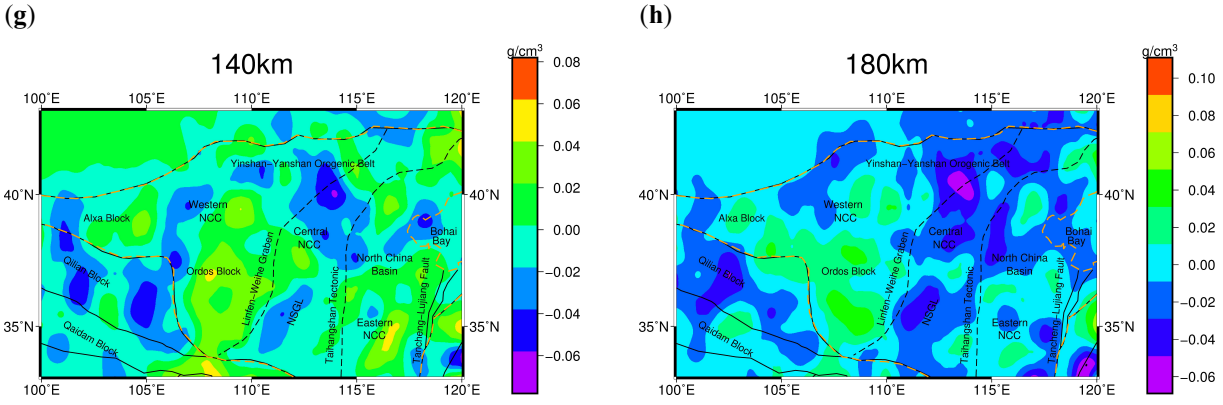

Figure 6 Lithospheric density distribution of NCC by gravity, HFS Haiyuan fault system, RMF Riyue mountain fault, SP Songliao plain. (**a**)10 km depth. (**b**)25 km depth. (**c**)42 km depth. (**d**)60 km depth. (**e**)80 km depth. (**f**)100 km depth. (**g**)140 km depth. (**h**)180 km depth.

3.2 Obtain GOCE satellite data for study area

The GOCE L2 (GOCE GO_CONS_EGG_TRF_2) gravity gradient measurement product provided for users includes the gravity gradient data along the orbit of the satellite. This study directly downloads the preprocessed gravity gradient anomaly data with the spatial resolution of 10 arc-min, acquired over 48 months from November 2009 to October 2013 (Sebera et al., 2014), from the website GOCE+ Geoexplore II of the European Space Agency (http://goce.kma.zcu.cz/). These data has undergone average orbit height correction (Sebera et al., 2014) and normal gravity gradient correction (Šprlák, 2012). The geographic area within E100°–E120° and N33°–N43° is defined as the study area (Fig. 7a–d), where the area of NCC is located.

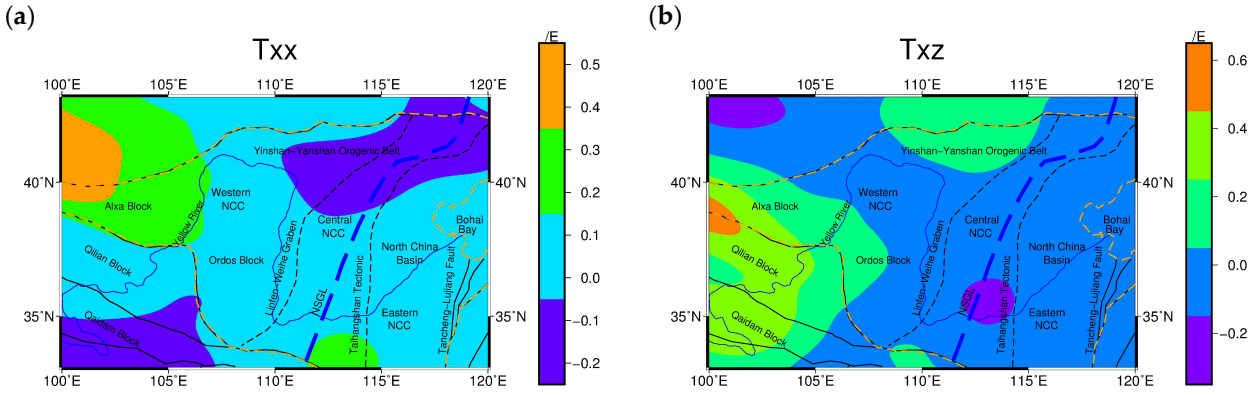

https://doi.org/10.5194/se-2019-181
Preprint. Discussion started: 2 January 2020

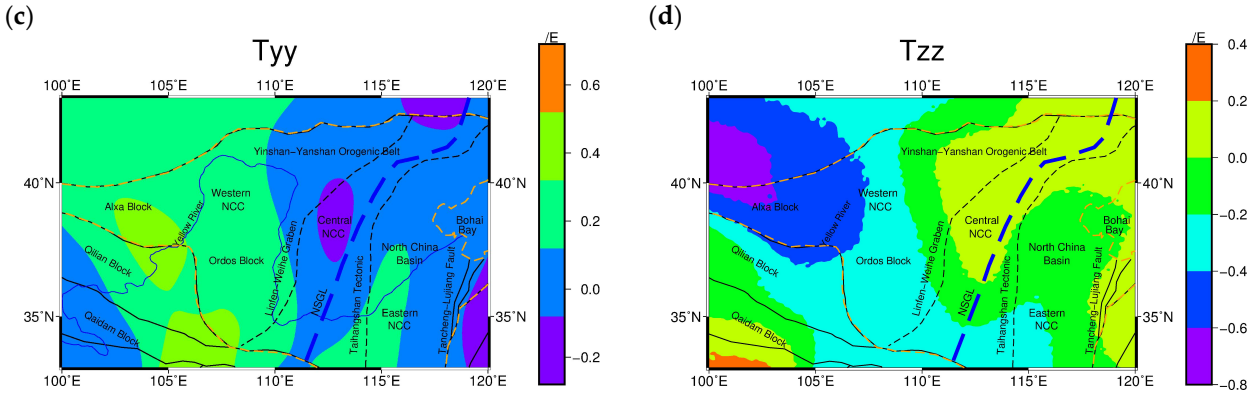

Figure 7 The gravity gradient anomaly after average orbital correction to the altitude of 250km. (**a**) $\boldsymbol{T}_{xx}$. (**b**) $\boldsymbol{T}_{xz}$. (**c**) $\boldsymbol{T}_{yy}$. (**d**) $\boldsymbol{T}_{zz}$.

3.3 Downward continuation

The data of the GOCE satellite at the average orbit height only reflect the long wavelength information and the large structure features inside the earth. To highlight the high frequency information of the shallow anomaly body and detailed information of the structural features, such as depth and shape, the GOCE satellite data at the average orbit height for the NCC have been downward continued to the near surface area. The obtained results benefits for the lithospheric structure analysis for local areas. The software Tesseroids developed by Uieda et al. (2016) is used in the calculation of the topography and the underground interface undulation effects. To ensure the accuracy of the calculation, the software recommends a distance of at least 1 km between the observation plane and the mass body, while the highest point of the topography in the study area is located at approximately 5 km. Thus, the gravity gradient components are downward continued to 10 km above the geoidal surface (Fig. 8a–d). The iterative continuation methods based on the Poisson approximate integration theory, specifically developed for satellite gravity gradient components by Sebera et al. (2014), are adopted, in which the space outside the earth surface is regarded to be mass free.

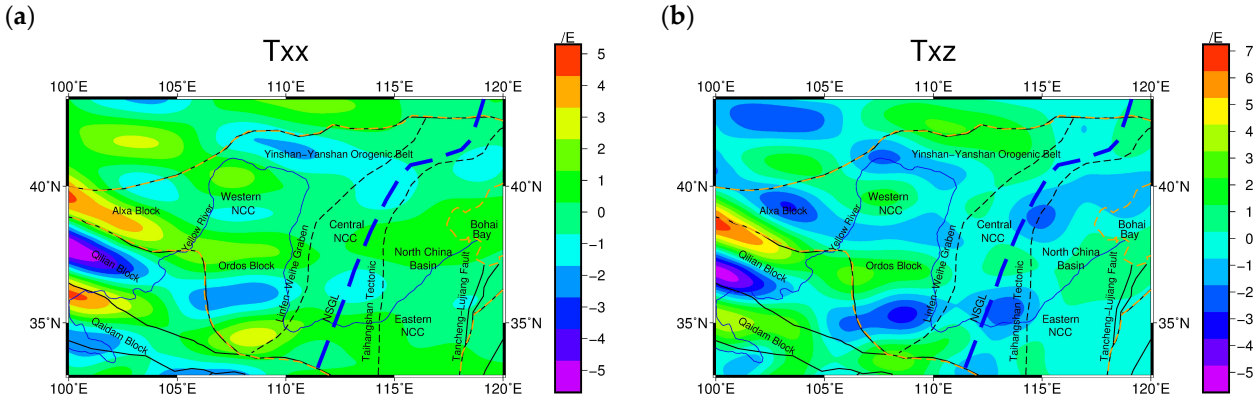

https://doi.org/10.5194/se-2019-181
Preprint. Discussion started: 2 January 2020

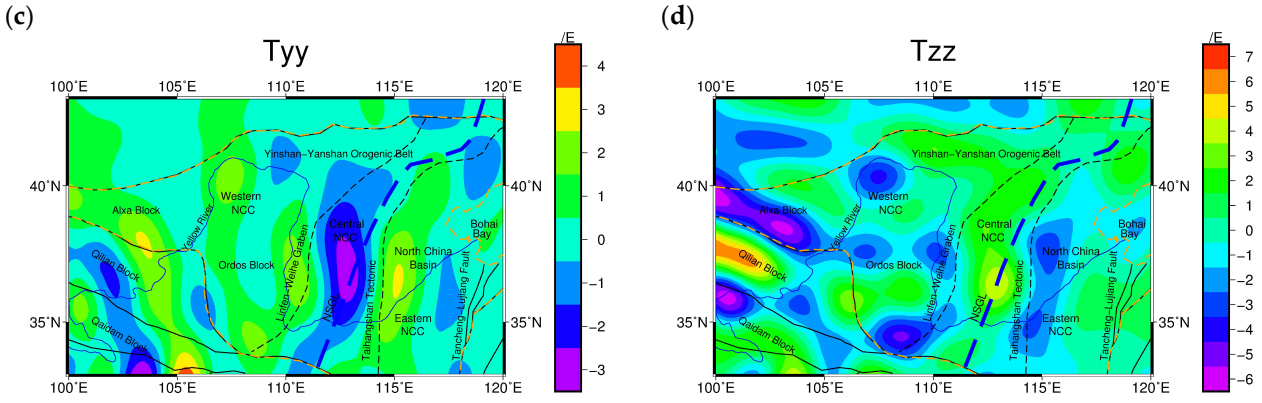

Figure 8 The gravity gradient effect after downward continuation to the altitude of 10km. **(a)** T_{xx} . **(b)** T_{xz} . **(c)** T_{yy} . **(d)** T_{zz} .

3.4 Correction for the topographic effects

The gravity gradient anomaly components after downward continuation are a combination of the interface undulation and density heterogeneity. Thus, the topographic correction, underground interface undulation correction and long wavelength correction should be carried out in accordance with the existing precise model.

First, the topography effects are calculated using the software Tesseroids (https://tesseroids.readthedocs.io/en/latest) developed by Uieda et al. (2016), which is aimed at deducting the gravity anomaly induced by the topographic mass above the geoidal surface from the gravity gradient after continuation. The software Tesseroids is able to convert the spherical hexahedron(tesseroid) in the spherical coordinate into the prism in the Cartesian coordinate to calculate the corresponding gravity gradient effects for topography. The software Tesseroids provides the built-in module to calculate the topography effects, for which the calculation is based on the topography elevation data ETOPO1 with the spatial resolution of 1′ × 1′(Amante and Eakins 2009). In order to directly reveal the correlation between the topography and the calculated gravity gradient effects. The resultant three dimensional model is shown in Fig. 9e, where the interface undulation represents the topography(Fig. 1), and the colour reflects the gravity gradient effects T_{zz} (Fig. 9d) .

https://doi.org/10.5194/se-2019-181
Preprint. Discussion started: 2 January 2020

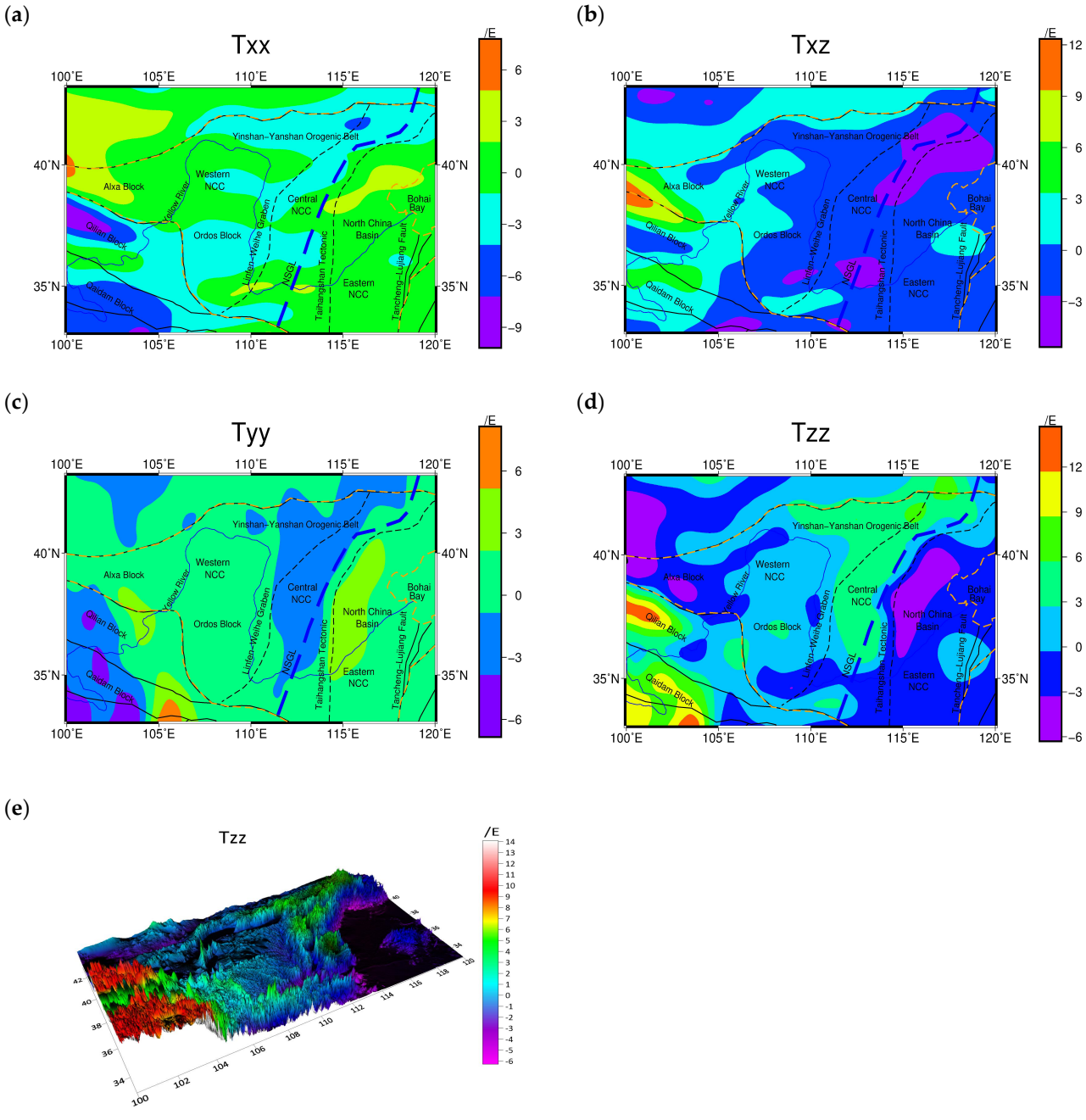

400 **Figure 9** The gravity gradient effect caused by the topographic masses. (**a**) $\boldsymbol{T}_{xx}$. (**b**) $\boldsymbol{T}_{xz}$. (**c**) $\boldsymbol{T}_{yy}$. (**d**) $\boldsymbol{T}_{zz}$. (**e**)The 3D overlay model map.

https://doi.org/10.5194/se-2019-181
Preprint. Discussion started: 2 January 2020

Solid Earth
Discussions
Open Access
EGU

3.5 Correction for the underground interface undulation effects

First, the average depth and density of the sediment in this area should be calculated for the interface undulation effects. The average depth is calculated from the depth data of the sediment in NCC (Fig. 10a) provided by CRUST 1.0 with the spatial resolution of 1° × 1° (Laske et al., 2013), and then the interface undulation data of the sedimentary layer (Fig. 10b) are obtained after correcting for the average sedimentary layer depth. With respect to the calculated average depth, all the density data corresponding to the average depth are extracted in order to calculate the average density corresponding to the average sedimentary layer depth. The average sedimentary layer depth in NCC is calculated to be 2.3 km, and the corresponding average density is 2.45 g/cm ^{3}. Moreover, the differences in the depth and density at each point from the average depth and density are calculated using the tesseroid forward modelling method based on the software Tesseroids. Consequently, the gravity gradient effects induced by the sedimentary layer undulation in NCC are obtained (Fig. 10c–f). To more intuitively illustrate the correlation between the sedimentary layer interface undulation and the calculated gravity gradient effects, in Fig. 10g, the interface undulation denotes the sedimentary layer interface undulation(Fig. 10b), and the contour lines represent the corresponding gravity gradient effects $\boldsymbol{T}_{zz}$ (Fig. 10f) .

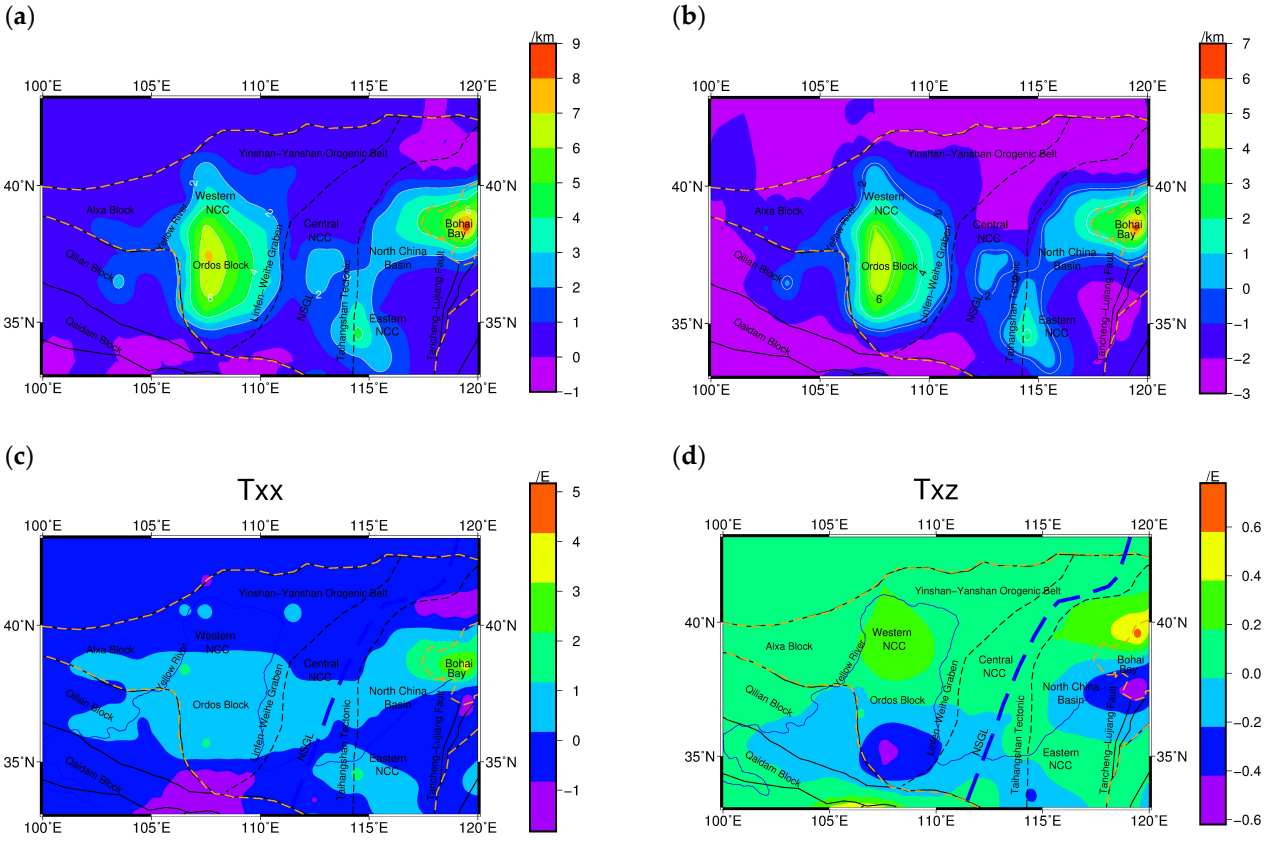

https://doi.org/10.5194/se-2019-181
Preprint. Discussion started: 2 January 2020

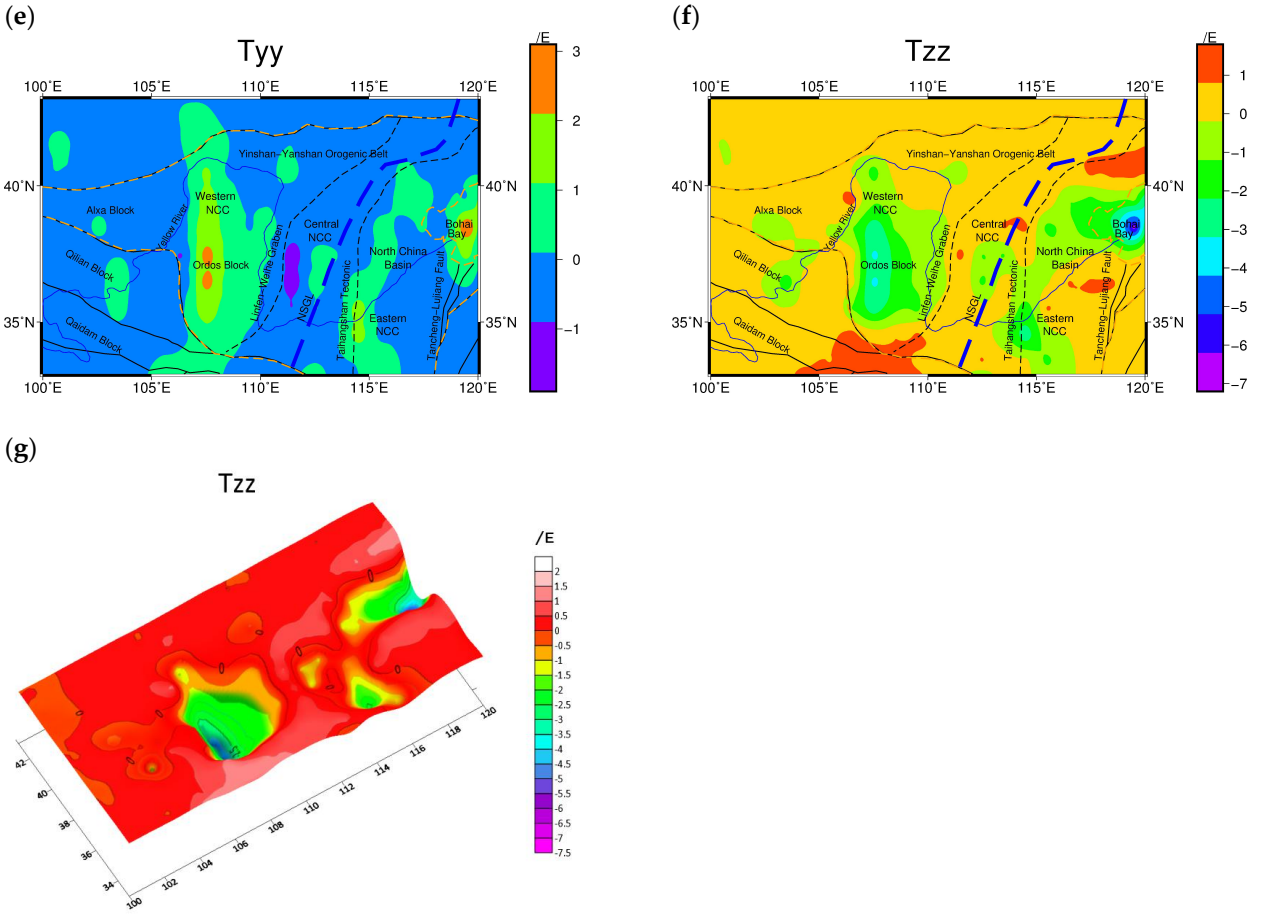

Figure 10 (**a**) Sedimentary layer interface of the NCC. (**b**) Sedimentary layer interface fluctuation of the NCC. (**c**) The anomalous gravity gradient component T_{xx} caused by the relief at the sedimentary layer interfaces. (**d**) The anomalous gravity gradient component T_{xz} caused by the relief at the sedimentary layer interfaces. (**e**) The anomalous gravity gradient component T_{yy} caused by the relief at the sedimentary layer interfaces. (**f**) The anomalous gravity gradient component T_{zz} caused by the relief at the sedimentary layer interfaces. (**g**) The 3D overlay model map.

Similarly, the gravity gradient effects induced by the Moho discontinuity can be calculated. The calculation results show that the average depth of the Moho discontinuity is 36.5 km and that the corresponding average density is 3.32 g/cm^3. The depth of the Moho discontinuity is shown in Fig. 11a, and the Moho discontinuity undulation after correcting for the average depth is illustrated in Fig. 11b. The gravity gradient effects induced by the Moho discontinuity undulation based on the Tesseroids software are presented in Fig. 11c–f. The resultant three dimensional model is shown in Fig. 11g, where the interface undulation reflects the Moho undulation(Fig. 11b) and the contour line represents the gravity gradient effects (Fig. 11f).

https://doi.org/10.5194/se-2019-181
Preprint. Discussion started: 2 January 2020

Solid Earth
Discussions
Open Access
EGU

(a)

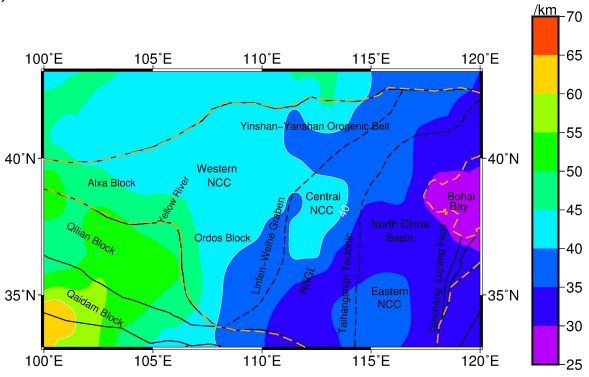

(b)

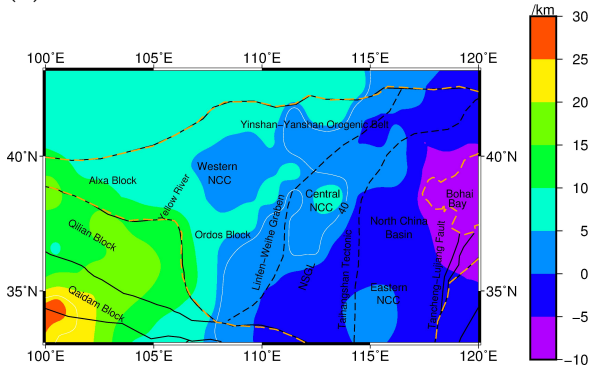

(c)

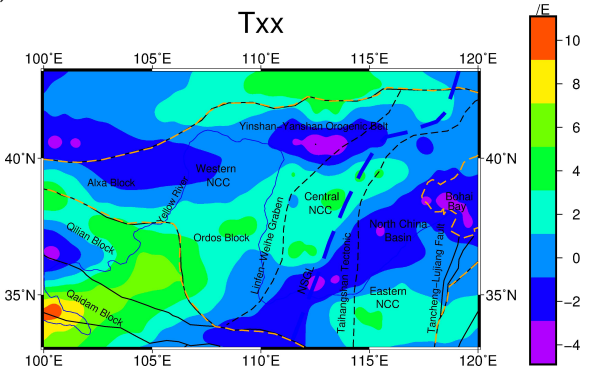

(d)

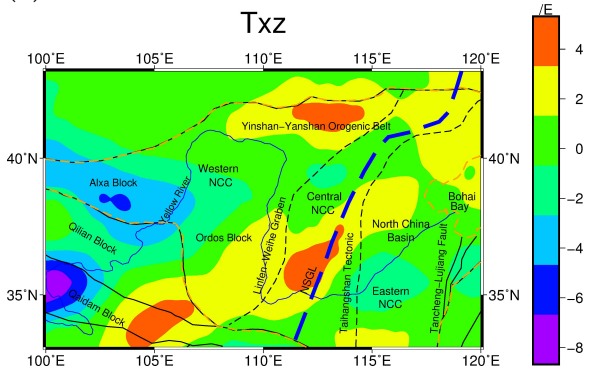

(e)

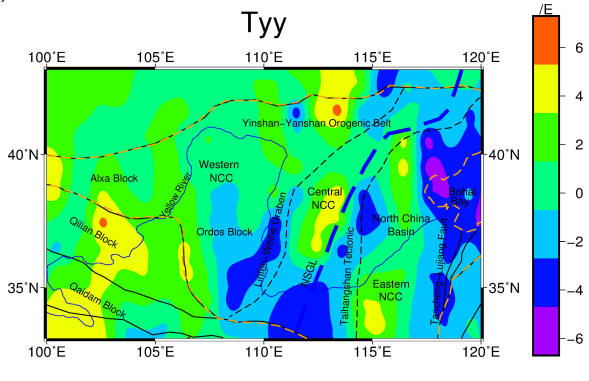

(f)

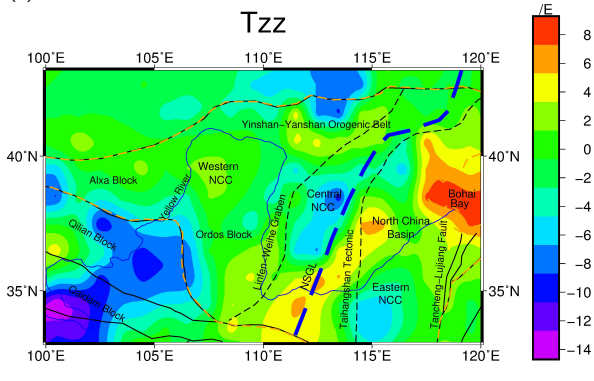

https://doi.org/10.5194/se-2019-181
Preprint. Discussion started: 2 January 2020

(g)

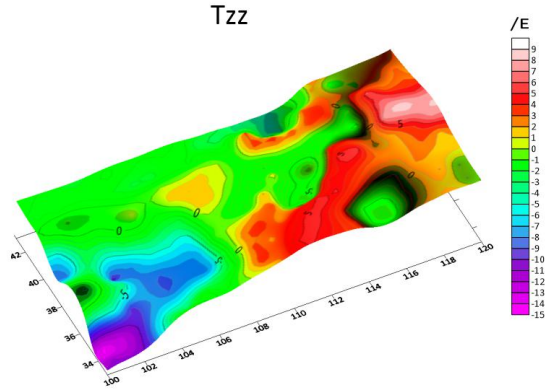

Figure 11 (**a**) Moho layer interface of the NCC. (**b**) Sedimentary layer interface fluctuation of the NCC. (**c**) The anomalous gravity gradient component T_{xx} caused by the relief at the Moho layer interfaces. (**d**) The anomalous gravity gradient component T_{xz} caused by the relief at the Moho layer interfaces. (**e**) The anomalous gravity gradient component T_{yy} caused by the relief at the Moho layer interfaces. (**f**) The anomalous gravity gradient component T_{zz} caused by the relief at the Moho layer interfaces. (**g**) The 3D overlay model map.

3.6 Correction for the long wavelength effects

The long wavelength gravity gradient effects are mainly induced by substance density heterogeneity in the lithosphere at depths deeper than 180 km. The correlation between the depth of the field source and the order of the spherical harmonic function of the gravity potential developed by Bowin et al. (1986) is adopted:

$$Z=R/(n-1) \quad (17)$$

where Z is the depth of the field source; R is the radius of the Earth; and n is the order of the spherical harmonic function. The long wavelength gravity gradient anomalies effects corresponding to the 2nd–33th order spherical harmonic coefficients(Wang et al., 2014) in the EGM 2008 are calculated. The gravity gradient effects induced by the long wavelength are relatively minor, as is shown in Fig. 12.

(a)

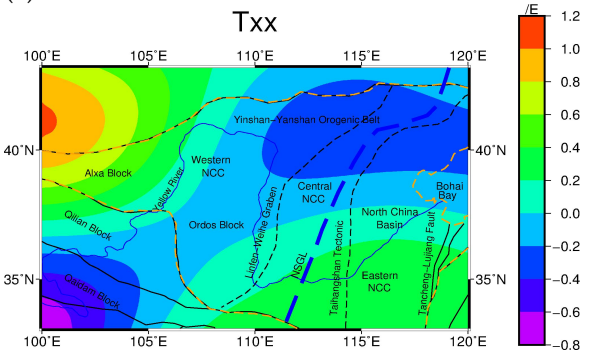

(b)

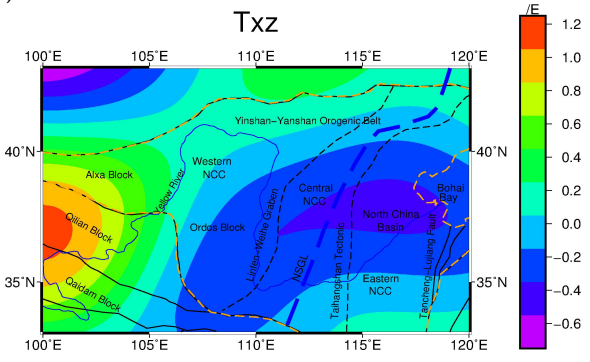

https://doi.org/10.5194/se-2019-181
Preprint. Discussion started: 2 January 2020

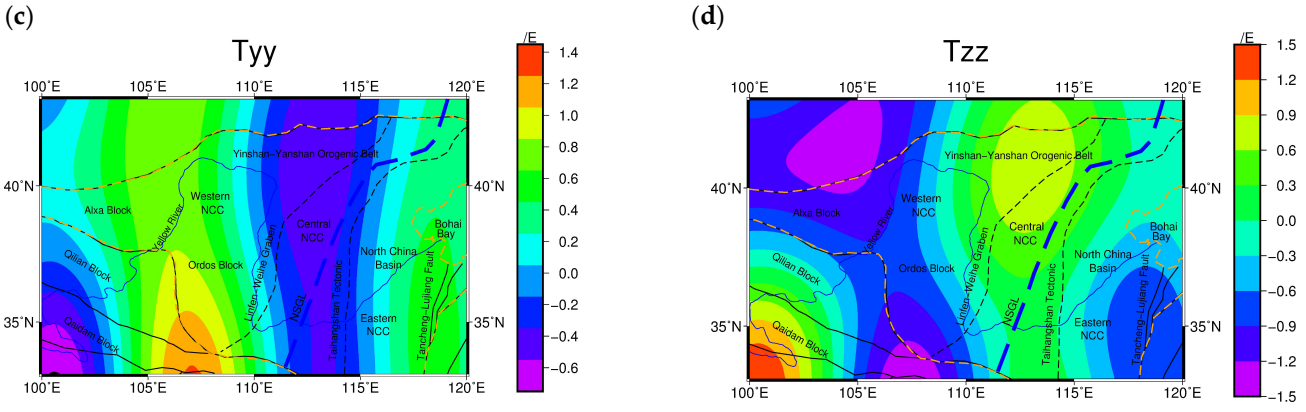

Figure 12 The gravity gradient effect caused by the long wavelength correction. (**a**) T_{xx} . (**b**) T_{xz} . (**c**) T_{yy} . (**d**) T_{zz} .

3.7 Remaining gravity gradient components

For the accuracy and reliability of each gravity gradient effect corrections, the data used for the calculations are same with the official website downloaded data. However, since different models are used, the spatial resolutions of the obtained results are different. Therefore, before calculating the remaining gravity gradient component, the resolutions of the results for each calculation are unified to 0.25° × 0.25°. The remaining gravity gradient anomaly components (Fig. 13) are obtained after deducting topography effects, the underground interface undulation effects and the long wavelength effects from the gravity gradient tensor data after downward continuation.

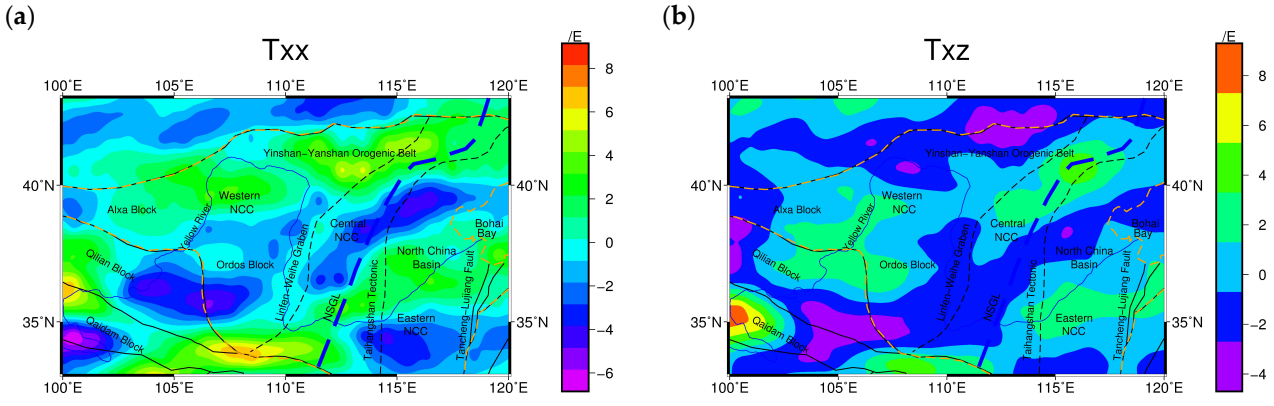

https://doi.org/10.5194/se-2019-181
Preprint. Discussion started: 2 January 2020

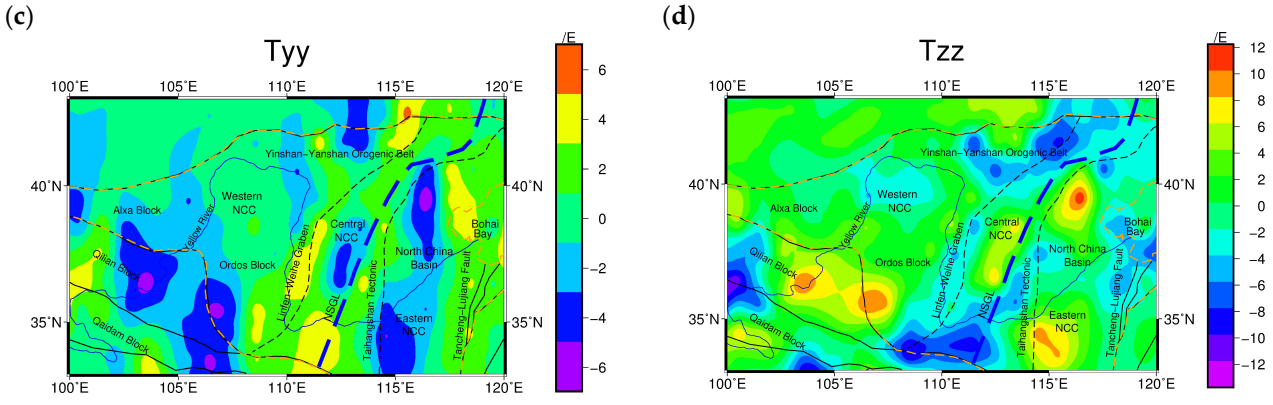

Figure 13 The remaining gravity gradient components. (**a**) $\boldsymbol{T}_{xx}$. (**b**) $\boldsymbol{T}_{xz}$. (**c**) $\boldsymbol{T}_{yy}$. (**d**) $\boldsymbol{T}_{zz}$.

4 Results

In Fig. 14, after 8 outer iterations, the curve of defined RMS misfit tends to be horizontal, the variation is more and more slight between the values of defined RMS misfit, an calculated RMS misfit of 9.0×10^{-3} was obtained, at which point the inverse iterative computation was complete. As shown in the inversion results (Fig. 15), an obvious heterogeneity is present in both the horizontal and vertical distributions of the lithospheric density within the NCC, and it is specifically featured by a segmented spatial distribution of the lithospheric density. In comparison (Fig. 6), inversion based on the gravity gradient provides more local and detailed information about the density anomaly distribution within the entire NCC at the depth of 0-100 km , which is more favourable for the analysis and discussion of the local density distribution.

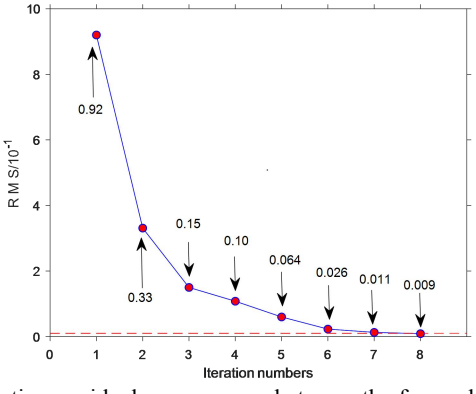

Figure 14 With the iterative calculation, residual mean square between the forward calculated theoretical gravity gradient and the gravity gradient measurements versus iteration number in the PCG inversion algorithm, the red line represents the RMS value of 0.01.

https://doi.org/10.5194/se-2019-181
Preprint. Discussion started: 2 January 2020

5 Discussion

In general, obvious density anomalies at a depth of 10 km are only seen in the eastern and central areas of the NCC. At the depth of 25-40 km, significant negative density anomalies are present in the Taihang Orogenic belt along the central NCC, also the Qilian and Qaidam blocks along the western NCC. The significant high density anomalies exist in the Ordos block. For the depth of 60-80 km, low density anomalies are found in the Bohai Bay area in the eastern NCC, while widely distributed low density anomalies are seen in the Yinshan Orogenic belt. At a depth of 100 km, the entire NCC is characterized by spatially alternating positive and negative density anomalies. In comparison, at the depth of 140-180 km, an obvious regional differentiation in the density anomaly distribution is seen, obvious low density anomalies in the Datong volcano at the junction of the Yinshan-Yanshan Orogenic and the Taihang Orogenic belt in the eastern NCC, as well as the Qilian block at the junction of the Qaidam and Ordos blocks in the western NCC.

According to the horizontal spatial distribution of the lithospheric density, the NCC is divided into three main areas, namely, the eastern NCC, consists of the North China Basin and the Bohai Bay area; the central NCC, consists of the central transitional belts; and the western NCC, consists of the Ordos Basin and its surrounding areas. Moreover, the density anomaly distribution characteristics in each area at different depths are discussed, based on the local density anomalies areas in Fig. 15a-h.

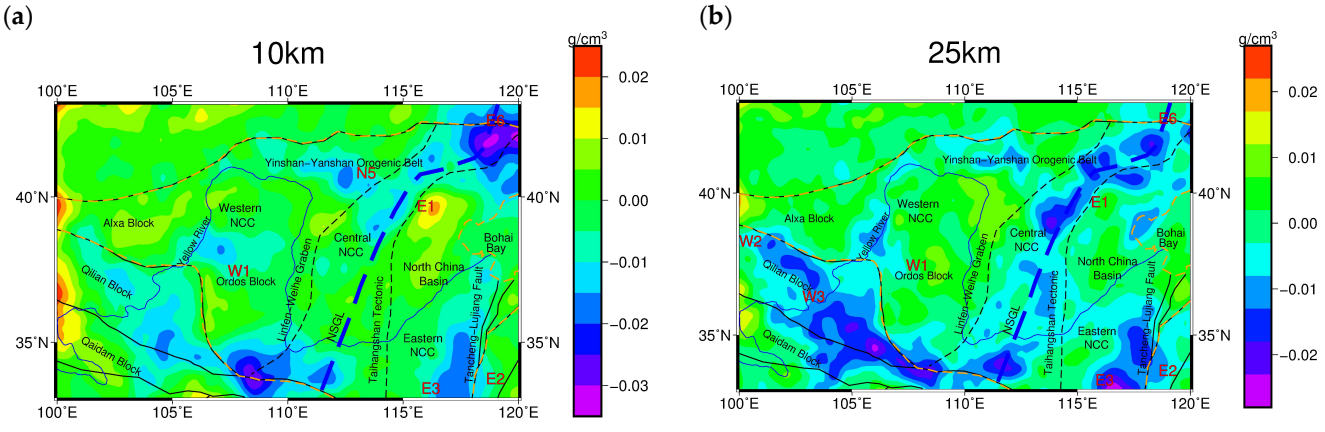

https://doi.org/10.5194/se-2019-181
Preprint. Discussion started: 2 January 2020

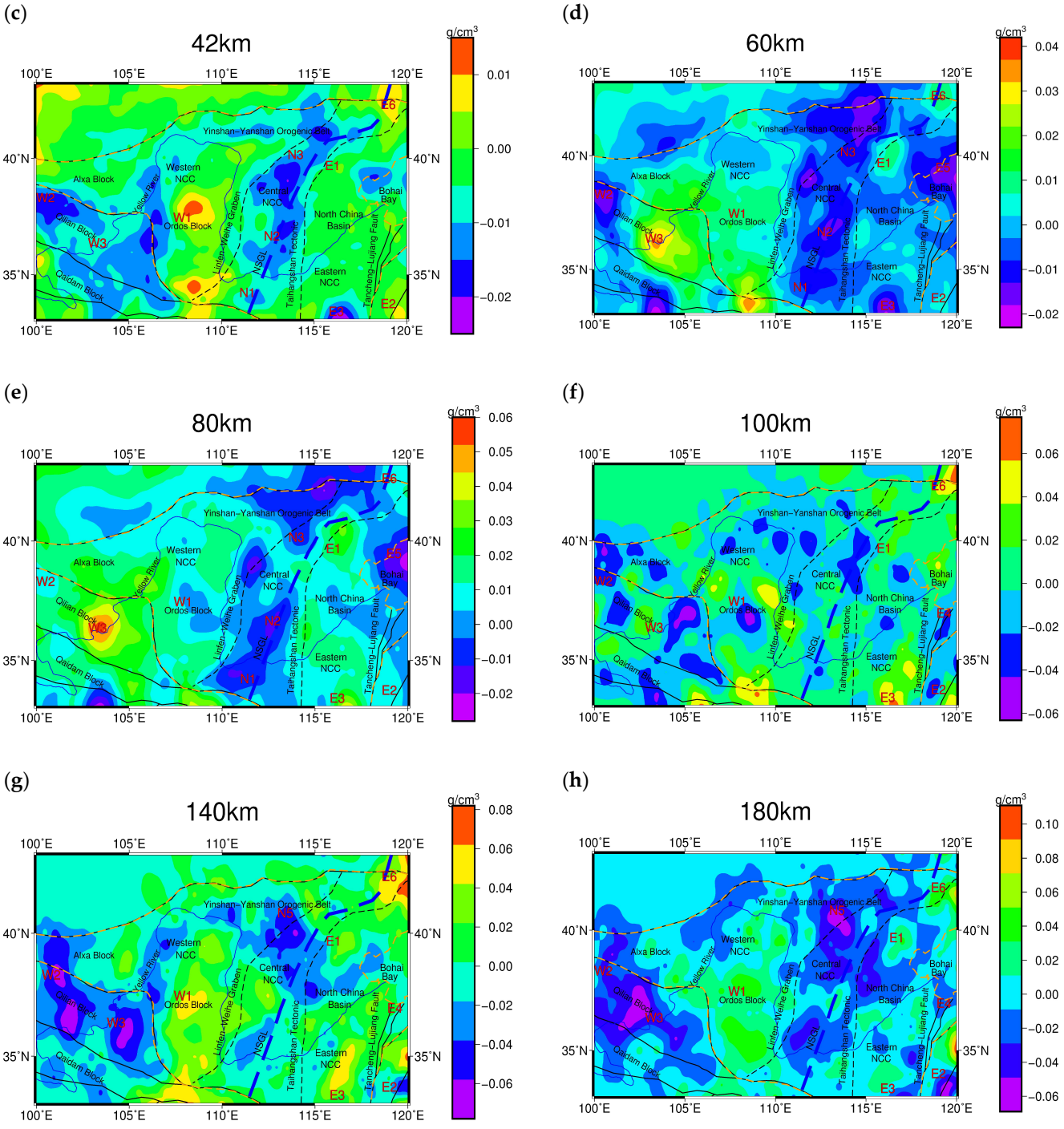

485 **Figure 15** Lithospheric density distribution of NCC. HFS Haiyuan fault system, RMF Riyue mountain fault, SP Songliao plain. E represents eastern NCC, N represents Central NCC, W represents western NCC. (**a**)10 km depth. (**b**)25 km depth. (**c**)40 km depth. (**d**)60 km depth. (**e**)80 km depth. (**f**)100 km depth. (**g**)140 km depth. (**h**)180 km depth.

https://doi.org/10.5194/se-2019-181
Preprint. Discussion started: 2 January 2020

5.1 Eastern NCC

The Eastern NCC is characterized by obvious features with connections to the Bohai Bay. The clearly obvious spatial distributions of the density anomalies are consistent with the theory that this area has experienced strong deformation (Tian and Zhao, 2011).

At a depth interval of 10-180 km in the Eastern NCC, there are positive density anomalies in the E1 area of the North China Basin, which are mainly distributed along the Beijing-Baoding direction. The result is consistent with the Tangshan-Xingtai earthquake belt through the research by Huang and Zhao (2009) on the P-wave velocity.

The Tancheng-Lujiang fault belt in the Eastern NCC is extended in the North-Northeast direction, on both sides of which (the E2 area in the right and the E3 area in the left) density anomalies are significantly different, the density anomalies along the Tancheng-Lujiang fault belt extend down to the depth of 180 km. At a depth of 42 km, significant positive density anomalies are present in the E3 area as the locally extreme value, while regional positive density anomalies are observed in the E2 area (Fig. 15c). At a depth of 80 km, significant positive density anomalies are present in the E3 area, while no density anomalies are observed in the E2 area (Fig. 15e). At a depth of 100-180 km, the density anomalies are obvious (Fig. 15h), including those in the E3 area with a direction consistent with the fault belt strike and those in the E2 area with alternating distributions of positive and negative density anomalies. Moreover, these positive and negative density anomalies are the local extremes, reaching 0.10 g/cm^3 and -0.06 g/cm^3, respectively. The inversion results demonstrate persistently present significant differences in the density distribution of the blocks on both sides of the Tancheng-Lujiang fault belt, which indicates that the fault belt may have penetrated the lithosphere.

In the E5 area of the Bohai Bay, there are no significant negative density anomalies at the depth of 60-80 km. This area is featured by the columnar shape density distribution at a depth of 80 km. However, with the depth increasing from 100 km to 180 km, there are no continuous regional negative density anomalies in the E5 area. In contrast, distinct low density anomalies are seen in the E4 area, which is in the extended region of the Tancheng-Lujiang fault belt. Meanwhile, density anomalies are seen in the extended region of the major fault belt in the adjacent area of the eastern boundary of the Tancheng-Lujiang fault belt. According to previous studies (Teng et al., 1997; Su et al., 2009), these density anomalies are ascribed to the extension of the Tancheng-Lujiang fault belt and the development of the mantle plume in the deep Bohai Bay area. In contrast, this study suggests a limited influence of the mantle plume and proposes an extension of the major fault belt in the adjacent area of the eastern boundary of the Tancheng-Lujiang fault belt as the main reason.

In the E6 area, which is a transitional area between the Yanshan block and the Songliao Basin, significant low density anomalies are present at a depth of 10 km (Fig. 15a). As the depth increases, persistent high density anomalies are seen in the upper mantle, especially at a depth range of 100-140 km, with the value reaching up to 0.07-0.08 g/cm^3. Moreover, the

https://doi.org/10.5194/se-2019-181
Preprint. Discussion started: 2 January 2020

density anomalies are aligned in the southwest direction at depths of 140-180 km relative to those at depths of 0-100 km. This phenomenon is attributed to the southwest extension of the high density mantle lithosphere below the Songliao Basin, reaching the region below the Yanshan Orogenic belt.

5.2 Central NCC

The Central NCC, formed by the central transitional zone, is characterized by significant low density anomalies with obvious segmented distributions. The Taihang Orogenic belt is generally northeast-southwest oriented, and it can be divided into three blocks, namely, the southern block N1, the middle block N2, and the northern block N3, all of which present different dimensions and distributions in terms of density anomalies at the same depth interval. From 25 km to 100 km, N1 is connected to the high density anomaly area of the western NCC, N2 is adjacent to the high density anomaly area of the eastern NCC, the eastern part of N3 is connected to the high density anomaly area of the North China Basin, and the western part of N3 is adjacent to the low density anomaly area in the Yinshan-Yanshan blocks, forming large scale low density anomaly areas. These characteristics at different areas may indicate the different geological processes that the southern, northern and central parts of the Taihang Orogenic belt have experienced.

The Linfen-Weihe Graben block is mainly characterized by alternating high and low density anomalies. N4 in the northern part of the Linfen-Weihe Graben block is mainly distributed in the Datong volcanic area. As the depth increases, the density anomalies significantly becomes high density anomalies at 25 km (Fig. 15b), and then becoming low density anomalies from 42 km to 180 km. Although the Datong volcano is no longer active (Tian et al., 2009), its surrounding area still exhibits low density anomalies.

N5 in the Yinshan-Yanshan area is featured by obvious low density anomalies at depths of 10-25 km, where are high density anomalies. In general, these anomalies are shallow and mainly distributed along the orogenic belt. Granite bodies along the orogenic belt are thought to be the main reason to these low density anomalies. As the depth increases to 60 km (Fig. 15d), these anomalies become connected with N3 in the north of the Taihang Orogenic belt and with N4 at the junction of the Linfen-Weihe Graben block, forming a large low density anomaly zone. As the depth further increases, the low density anomaly area covering N5 presents persistently negative density anomalies that extend down to a depth of 180 km (Fig. 15h). Moreover, the negative density anomaly value is more significant. Because the central NCC is located in the orogenic belt with the high mantle temperature (An and Shi, 2007; Yang et al. 2013), which implies that the temperature and material composition seem to have a dominant influence. The presence of a high heat flux environment is accompanied by the upwelling of hot materials in the deep asthenosphere, which transforms the lithospheric mantle.

https://doi.org/10.5194/se-2019-181
Preprint. Discussion started: 2 January 2020

N6 in the central NCC exhibits significant positive density anomalies, which contrast the low density anomalies over a large area of the central NCC. The crustal part of N6 is connected to the positive density anomaly area in the eastern NCC, while its mantle part is connected to the positive density anomaly area in the W1 area, Ordos block, western NCC (Fig. 15e-f). Therefore, it is inferred that the central NCC in the crustal part is affected by the thinning of the eastern lithosphere, while that in the mantle part experiences the blocking effect by the rigid Ordos block during expansion of the orogenic belt.

5.3 Western NCC

Strong tectonic deformation and significant magmatic activities since the Mesozoic and Cenozoic have resulted in the complex tectonic patterns in the Ordos block and its surrounding areas (Zhang et al., 2011). The Ordos block is surrounded by the Yinchuan-Hetao and Shaanxi-Shanxi rift valleys, and it is overall a stable tectonic unit.

At a depth of 42 km, the W1 area in the central Ordos block is characterized by high density anomalies (Fig. 15c), whereas no obvious anomalies are seen in the northern part of the Ordos block. According to the receiver function (Tian and Zhao, 2011), the central part of the Ordos block is 41 km thick, which thickens to 45 km in the northern part. Therefore, it can be inferred that the southern part of the Ordos block has entered the lithospheric mantle at a depth of 42 km. From 60 km to 100 km, the high density anomalies in the W1 area of the central Ordos block gradually change to low density anomalies. At the depth interval of 140-180 km, the high density anomalies still dominate the W1 area of the central Ordos block. Meanwhile, the low density anomaly area at depths of 60-100 km is connected to the negative density anomaly areas in the Taihang Orogenic belt and the Qilian block on both sides. Therefore, it can be inferred that the density anomalies in the central Ordos block are influenced by the deep dynamic processes involved in the development of the Taihang Orogenic belt and the Qilian block.

The whole Qilian block (W2 and W3 areas) is featured by significant low density anomalies in the crustal part at 25-40 km, which falls in the range of the Haiyuan fault belt. The boundary of the negative density anomalies is essentially consistent with the strike of the fault belt shown on the surface. The W3 area at the junction of the Qilian and Ordos blocks is characterized by a sharp transition from low density to significant high density. At a depth of 25-80 km, the density anomalies in the Qilian block present a dominant NW-SE strike; however, this strike turns clockwise to the NS direction as the depth further increases to 180 km, especially after entering the mantle. This observation is consistent with previous research results in this region. The mantle convective stress field calculated based on gravity anomalies is demonstrated to be significantly inconsistent with the crustal movement pattern (Xiong and Teng, 2002; Wang et al., 2013), which indicates obvious decoupling between the crustal and mantle materials in the Qilian block. The Qilian block is located at the junction of the north-eastern Qinghai-Tibet plateau and the Alashan and Ordos blocks in the western NCC. The Qilian block has not only been influenced by a collision and subduction of the Indian plate, but also by the blocking effect of the Ordos Block,

https://doi.org/10.5194/se-2019-181
Preprint. Discussion started: 2 January 2020

585 which resulting in the strong regional tectonic stress background in the deep part of the Qilian block with an associated clockwise rotation of the material movement.

As the depth increases in the range of 140-180 km, persistent obvious negative density anomalies are increasingly dominant in the Qilian block in the western NCC and at the junction of the Taihang Orogenic belt and the Yinshan-Yanshan Orogenic
590 belt in the eastern NCC. According to the previous study (Teng et al., 2010), the lithosphere in the western NCC is the thickest, with an average depth of 140-150 km. However, within this depth range, two obvious low density anomalies are present in the orogenic belts of the eastern and western NCC, which eliminates the possibility that the lithospheric thinning is the main cause of the density anomalies at a depth of 140-180 km. However, according to the temperature distribution in the crust and the upper mantle of the entire NCC (Yang et al., 2013), the inversion results indicate the persistent location of the
595 junction of the Taihang Orogenic belt and the Yinshan-Yanshan Orogenic belt in the high heat flux environment. Specifically, the mantle temperature at this junction is also relatively high. The mantle part of the asthenosphere below 150 km in the western NCC has a higher temperature than that in the eastern NCC. Furthermore, according to research on the terrestrial heat flux (An and Shi, 2007), the Qilian block has an average heat flux value up to 68.340 mW/m^2. Therefore, it can be concluded that the high heat flux environments lead to negative density anomalies in the Qilian Block in the western
600 NCC and at the junction of the Taihang Orogenic belt and the Yinshan-Yanshan Orogenic belt in the eastern NCC, accompanied by an upwelling of deep asthenosphere materials and the subsequent transformation of the mantle above the lithosphere.

6 Conclusions

The joint inversion of the lithosphere density structure in the NCC are divided into two stages. The effects of the initial
605 density model are taken into consideration. The inversion results obtained by the inversion of remaining gravity anomaly are used as the initial model for the inversion of the GOCE satellite gravity gradient components. The GOCE satellite gravity gradient data were processed with several corrections to obtain the remaining gravity gradient components. The density distribution with the depth range of 0-180km in NCC shows that: (1) In eastern NCC, affected by lithosphere thinning, the eastern NCC is seen with local features in the density anomaly distribution. Obvious differences in the density anomaly
610 distribution are observed, and the Tancheng-Lujiang fault belt in the eastern NCC penetrates through the lithosphere. The density anomaly in the Bohai Bay is mainly induced by the extension of the Tancheng-Lujiang major fault at the eastern boundary. (2) In central NCC, the Taihang Orogenic belt located in the central NCC is characterized by a segmented density anomaly distribution. (3)In western NCC, the Qilian block in the western NCC presents a clockwise rotation of the density anomaly distribution with an increasing lithospheric depth, while the adjacent Ordos block remains continuously stable. (4)
615 Across the Taihang Orogenic belt in the central NCC and the Qilian-Qaidam blocks in the western NCC, stronger impacts of

https://doi.org/10.5194/se-2019-181
Preprint. Discussion started: 2 January 2020

the orogenic belt and a high heat flux environment are observed, which results in an upwelling of the deeply buried asthenospheric substances and, consequently, a reconstruction of the lithospheric density structure distribution.

Code and data availability. The on-orbit GOCE gravity gradient data can be browsed and downloaded from GOCE+ Geoexplore II(http://goce.kma.zcu.cz/). The software "Tesseroids" for gravity gradient topographic correction and interface undulation can be browsed and downloaded from https://tesseroids.readthedocs.io/en/latest. The global crustal model CRUST1.0 can be downloaded from https://igppweb.ucsd.edu/~gabi/crust1.html. The processed gravity gradient data and inversion results can be browsed and downloaded from https://zenodo.org/record/3545809#.XdJ5H695vIU.

Author contributions. Conceptualization, YW; methodology, YT; validation, YT, writing original draft preparation, YT; writing review and editing, YT; supervision, YW; funding acquisition, YW.

Competing interests. The authors declare no conflict of interest.

Acknowledgements. We are grateful to Prof. Xinsheng Wang in Development Research Center of China Earthquake Administration for providing remaining gravity data.

Financial support. This research was funded by the R&D of Key Instruments and Technologies for Deep Resources Prospecting (the National R&D Projects for Key Scientific Instruments), grant number No.ZDYZ2012-1-04.

https://doi.org/10.5194/se-2019-181
Preprint. Discussion started: 2 January 2020

References

Amante, C., and Eakins, B.W.: ETOPO1 1 arc-minute global relief model: Procedures, data sources and analysis, NOAA Technical Memorandum NESDIS NGDC-24, Boulder, Colorado, USA, March 2009, 19, 2009.

An, M.J., and Shi, Y.L.: Three-dimensional thermal structure of the Chinese continental crust and upper mantle, Sci. China Ser. D , Earth Sciences, 50(10), 1441-1451,doi:10.1007/s11430-007-0071-3, 2007.

Bowin, C., Scheer, E., and Smith, W.: Depth estimates from ratios of gravity, geoid, and gravity gradient anomalies, Geophysics, 51(1), 123-136, doi:10.1190/1.1442025, 1986.

Capriotti, J., and Li, Y. : Gravity and gravity gradient data: Understanding their information content through joint inversions, Proceedings of the 84th SEG Annual International Meeting, Denver, Colorado, USA, October 2014, 1329-1333, 2014.

Constable, S.C., Parker, R.L., and Constable, C.G.: Occam's inversion: A practical algorithm for generating smooth models from electromagnetic sounding data, Geophysics, 52(3), 289-300, doi:10.1190/1.1442303, 1987.

Fang, J.: Three-dimensional density distribution of lithosphere in North China, Geophys. Geochem. Explor., 23(3), 179-184, 1996.

Gao, S., Zhang, J.F., Xu, W.L., and Liu, Y.S.: Delamination and destruction of the North China Craton, Chinese Sci. Bull., 54, 3367-3378, doi:10.1007/s11434-009-0395-9, 2009.

Hansen, P.C.: Analysis of discrete ill-posed problems by means of the L-curve, Siam Rev., 34(4), 561-580, doi:10.1137/1034115, 1992.

Huang, J., and Zhao, D.: Seismic imaging of the crust and upper mantle under Beijing and surrounding regions, Phys. Earth Planet. In., 173(3-4), 330-348, doi:10.1016/j.pepi.2009.01.015, 2009.

Laske, G., Masters, G., Ma, Z., and Pasyanos, M.: Update on CRUST1.0-a1-degree global model of Earth's crust, Geophysical Research Abstracts, 15, Abstract EGU2013-2658, doi:10.6092/1970-9870/128, 2013.

Li, H., Shen, C., Sun, S., Wang, X., Xiang, A., and Liu, S.: Recent gravity changes in China Mainland, Geodesy Geodyn., 2(1), 1-12, doi:10.3724/SP.J.1246.2011.00001, 2011.

Li, H.L., Fang, J., Wang, X.S., Liu, J., Cui, R.H., and Chen, M.: Lithospheric 3-D density structure beneath the Tibetan plateau and adjacent areas derived from joint inversion of satellite gravity and gravity-gradient data, Chinese J. Geophys., 60(6), 2469-2479, doi:10.6038/cjg20170634, 2017.

Li, Y., and Oldenburg, D.W.: 3-D inversion of magnetic data, Geophysics, 61(2), 394-408, doi:10.1190/1.1443968,1996.

Liu, R., Wu, Z., Yin, C., Chen, Y., and Zhuang, C.: Development of China digital seismological observational systems, Acta Seismol. Sinica, 16(5), 568-573, doi:10.1007/BF02893477, 2003.

Pavlis, N.K., Holmes, S.A., Kenyon, S.C., and Factor, J.K. The development and evaluation of the Earth Gravitational Model 2008 (EGM2008), J. Geophys. Res.: Sol. Ea., 117, B04406, doi:10.1029/2011JB008916, 2012.

Pilkington, M.: 3-D magnetic imaging using conjugate gradients, Geophysics, 62(4), 1132-1142, doi:10.1190/1.1444214, 1997.

https://doi.org/10.5194/se-2019-181
Preprint. Discussion started: 2 January 2020

Pilkington, M.: 3D magnetic data-space inversion with sparseness constraints, Geophysics, 74(1), L7-L15, doi:10.1190/1.3026538, 2009.

Qin, P., Huang, D., Yuan, Y., Geng, M., and Liu, J.: Integrated gravity and gravity gradient 3D inversion using the non-linear conjugate gradient, J. Appl. Geophys., 126, 52-73, doi:10.1016/j.jappgeo.2016.01.013, 2016.

Rummel, R., Yi, W., and Stummer, C. : GOCE gravitational gradiometry, J. Geodesy, 85, 777-790, doi:10.1007/s00190-011-0500-0, 2011.

Sebera, J., Šprlák, M., Novák, P., Bezděk, A., and Vaľko, M.: Iterative spherical downward continuation applied to magnetic and gravitational data from satellite, Surv. Geophys., 35(4), 941-958, doi:10.1007/s10712-014-9285-z, 2014.

Šprlák, M.: A graphical user interface application for evaluation of the gravitational tensor components generated by a level ellipsoid of revolution, Comput. Geosci., 46, 77-83, doi:10.1016/j.cageo.2012.04.013, 2012.

Su, J., Zhu, W., Lu, H., Xu, M., Yang, W., and Zhang, Z.: Geometry styles and quantification of inversion structures in the Jiyang depression, Bohai Bay Basin, eastern China, Mar. Petrol. Geol., 26(1), 25-38, doi:10.1016/j.marpetgeo.2007.08.003, 2009.

Teng, J., Wang, F., Zhao, W., Zhang, Y., Zhang, X., Yan, Y., Zhao, J., Li, M., Yang, H., Zhang, H., and Ruan, X.: Velocity structure of layered block and deep dynamic process in the lithosphere beneath the Yinshan orogenic belt and Ordos Basin, Chinese J. Geophys., 53(1), 67-85, doi:10.3969/j.issn.0001-5733.2010.01.008, 2010.

Teng, J., Zhang, Z., Zhang, B., Yang, D., Wan, Z., and Zhang, H.: Geophysical fields and background of exceptional structure for deep latent mantle plume in Bohai Sea, Chinese J. Geophys., 40, 468-480, 1997.

Tian, Y., Ke, X., and Wang, Y.: DenInv3D: A geophysical software for three-dimensional density inversion of gravity field data, J. Geophys. Eng., 15(2), 354-365, doi:10.1088/1742-2140/aa8caf, 2018.

Tian, Y., Ke, X., and Wang, Y.: A folding calculation method based on the preconditioned conjugate gradient inversion algorithm of gravity gradient tensor, Pure Appl. Geophys., 176(1), 215-234, doi:10.1007/s00024-018-1965-z, 2019.

Tian, Y., and Wang, Y.: Inversion of the density structure of the lithosphere in the North China Craton from GOCE satellite gravity gradient data, Earth Planets Space, 70, 173, doi:10.1186/s40623-018-0942-1, 2018.

Tian, Y., and Zhao, D.: Destruction mechanism of the North China Craton: Insight from P and S wave mantle tomography, J. Asian Earth Sci., 42(6), 1132-1145, doi:10.1016/j.jseaes.2011.06.010, 2011.

Tian, Y., Zhao, D., Sun, R., and Teng, J.: Seismic imaging of the crust and upper mantle beneath the North China Craton, Phys. Earth Planet. In., 172(3-4), 169-182, doi:10.1016/j.pepi.2008.09.002, 2009.

Uieda, L., Barbosa,V.C.F., and Braitenberg, C.: Tesseroids: Forward-modeling gravitational fields in spherical coordinates, Geophysics, 81(5), 41-48, doi:10.1190/geo2015-0204.1, 2016.

Wang, X.S., Fang, J., and Hsu, H.: Density structure of the lithosphere beneath North China Craton, Chinese J. Geophys., 55(4), 1154-1160, doi:10.6038/j.issn.0001-5733.2012.04.011, 2012.

Wang, X.S., Fang, J., and Hsu, H.: 3D density structure of lithosphere beneath northeastern margin of the Tibetan Plateau, Chinese J. Geophys., 56(11), 3770-3778, doi:10.6038/cjg20131118, 10.1016/j.tecto.2013.11.002, 2013.

https://doi.org/10.5194/se-2019-181
Preprint. Discussion started: 2 January 2020

Wang, X., Fang, J., and Hsu, H.: Three-dimensional density structure of the lithosphere beneath the North China Craton and the mechanisms of its destruction, Tectonophysics, 610(6), 150-158,doi:10.1016/j.tecto.2013.11.002, 2014.

Wu, L., Ke, X., Hsu, H., Fang, J., Xiong, C., and Wang, Y.: Joint gravity and gravity gradient inversion for subsurface object detection, IEEE Geosci. Remote S., 10(4), 865-869, doi:10.1109/LGRS.2012.2226427, 2013.

Xiong, X., and Teng, J.W.: Study on crustal movement and deep process in eastern Qinghai-Xizang Plateau, Chinese J. Geophys., 45, 507-515, doi:10.1002/cjg2.266, 2002.

Xu, Y., Zeyen, H., Hao, T., Santosh, M., Li, Z., Huang, S., and Xing, J.: Lithospheric structure of the North China Craton: Integrated gravity, geoid and topography data, Gondwana Res., 34, doi:10.1016/j.gr.2015.03.010, 315-323, 2016.

Yang, S., Xiong, X., Zheng, Y., and Shan, B.: Upper-mantle temperature and lithospheric thickness of North China, Chinese J. Geophys., 56(11), 3855-3867,doi:10.6038/cjg20131127, 2013.

Yi, W., Rummel, R., and Gruber, T.: Gravity field contribution analysis of GOCE gravitational gradient components, Stud. Geophys. Geod., 57(2), 174-202, doi:10.1007/s11200-011-1178-8, 2013.

Zhang, Y., Teng, J., Wang, F., Zhao, W., Li, M., and Wang, Q.: Structure of the seismic wave property and lithology deduction of the upper crust beneath the Yinshan orogenic belt and the northern Ordos block, Chinese J. Geophys., 54(1), 87-97, doi:10.3969/j.issn.0001-5733.2011.01.010, 2011.

Zhdanov, M.S., Ellis, R., and Mukherjee, S.: Three-dimensional regularized focusing inversion of gravity gradient tensor component data, Geophysics , 69(4), 925-937, doi:10.1190/1.1778236, 2004.

Zhu, R.X., Yang, J.H., and Wu, F.Y.:Timing of destruction of the North China Craton, Lithos, 149(15), 51-60, doi:10.1016/j.lithos.2012.05.013, 2012.